Continuum Approach to Two- and Three-Phase Flow during Gas-Supersaturated Water Injection in Porous Media

by

Robert Enouy

A thesis

presented to the University of Waterloo

in fulfillment of the

thesis requirement for the degree of

Master of Applied Science

in

Chemical Engineering

Waterloo, Ontario, Canada, 2010

I hereby declare that I am the sole author of this thesis. This is a true copy of the thesis, including any required final revisions, as accepted by my examiners.

I understand that my thesis may be made electronically available to the public.

Abstract

Degassing and *in situ* formation of a mobile gas phase takes place when an aqueous phase equilibrated with a gas at a pressure higher than the subsurface pressure is injected in water-saturated porous media. This process, which has been termed supersaturated water injection (SWI), is a novel and hitherto unexplored means of introducing a gas phase into the subsurface. Herein is a first macroscopic account of the SWI process on the basis of continuum scale simulations and column experiments with CO_2 as the dissolved gas. A published empirical mass transfer correlation (Nambi and Powers, Water Resour Res, 2003) is found to adequately describe the non-equilibrium transfer of CO_2 between the aqueous and gas phases. Remarkably, the dynamics of gas-water two-phase flow, observed in a series of SWI experiments in homogeneous columns packed with silica sand or glass beads, are accurately predicted by traditional two-phase flow theory which allows the corresponding gas phase relative permeability to be determined. A key consequence of the finding, that the displacement of the aqueous phase by gas is compact at the macroscopic scale, is consistent with pore scale simulations of repeated mobilization, fragmentation and coalescence of large gas clusters (i.e., large ganglion dynamics) driven entirely by mass transfer. The significance of this finding for the efficient delivery of a gas phase below the water table in relation to the alternative process of *in-situ* air sparging and the potential advantages of SWI are discussed.

SWI has been shown to mobilize a previously immobile oil phase in the subsurface of 3-phase systems (oil, water and gas). A macroscopic account of the SWI process is given on the basis of continuum-scale simulations and column experiments using CO_2 as the dissolved gas and kerosene as the trapped oil phase. Experimental observations show that the presence of oil ganglia in the subsurface alters gas phase mobility from 2-phase predictions. A corresponding 3-phase gas relative permeability function is determined, whereas a published 3-phase relative permeability correlation (Stone, Journal of Cana Petro Tech, 1973) is found to be inadequate for describing oil phase flow during SWI. A function to predict oil phase relative permeability is developed for use during SWI at high aqueous phase saturations with a disconnected oil phase and quasi-disconnected gas phase. Remarkably, the dynamics of gas-water-oil 3-phase flow, observed in a series of SWI experiments in homogeneous columns packed with silica sand or glass beads, are accurately predicted by traditional continuum-scale flow theory. The developed relative permeability function is compared to Stone's Method and shown to approximate it in all regions while accurately describing oil flow during SWI. A published validation of Stone's Method (Fayers and Matthews, Soc of Petro Eng Journal, 1984) is cited to validate this approximation of Stone's Method.

Acknowledgements

I am very appreciative of the guidance, extensive advice, encouragement, and support from my supervisors, Dr. M. A. Ioannidis and Dr. A. J. Unger.

I would like to thank my lab mate Meichun Li for providing experimental data and advice leading to the completion of this project.

I also appreciate the support from Ralph Dickhout, Ravindra Singh, Jeff Gostick, Lesley James, and Dennis Herman.

Table of Contents

List of Figures

List of Tables

Nomenclature

$[-]$	[dim]	dimensionless
p		components: water (w), air (a), oil (o) and carbon dioxide (CO_2)
l		phases: aqueous (q), non-aqueous (n) and gas (g)
S_l	$[-]$	saturation of phase l
P_l	[kPa]	pressure of phase l
M_l	$[\mathrm{mole/m^3}]$	molar density of phase l
X_{pl}	$[-]$	mole fraction of component p in phase l
ρ_l	$[\mathrm{kg/m^3}]$	mass density of phase l
μ_l	$[\mathrm{kPa \cdot day}]$	viscosity of phase l
ϕ	$[-]$	porosity of porous media
$\mathbf{K}$	$[\mathrm{m^2}]$	Intrinsic permeability of porous media
k_{rl}	$[-]$	relative permeability of phase l
D_{pl}	$[\mathrm{m^2/day}]$	molecular diffusivity of component p in phase l
τ	$[-]$	tortuosity of porous media
α_L^l	[m]	longitudinal dispersivity of phase l
α_T^l	[m]	transverse dispersivity of phase l
Q_p	$[\mathrm{mole/(m^3 \cdot day)}]$	source (+ve) or sink (-ve) term for component p
Bo	$[-]$	Bond number
g	[m/s^2]	gravitational acceleration
$\Delta\bar{S}_g$	$[-]$	change in column-averaged gas saturation
$J(S_q)$	$[-]$	Leverett J-function
k_{rl}	$[-]$	relative permeability of phase l
k_{rncq}	$[-]$	oil relative permeability at connate water
k_{rnc}	$[-]$	critical oil relative permeability
n_l	$[-]$	relative permeability exponent of phase l
S_{lr}	$[-]$	irreducible saturation of phase l
P_{cgq}	[kPa]	capillary pressure between aqueous and gas phases
$\mathcal{S}_f$	$[-]$	super-saturation factor

$\Delta \mathcal{S}_f$	[−]	change in super-saturation factor
t_0	[min]	starting time of SWI experiment
t_{SWI}	[min]	end time of SWI experiment
t_{p-SWI}	[min]	end time of post-SWI experiment
$Q_g^{eff}(t)$	[mL/min]	experimental gas phase effluent rate
$Q_q^{inj}(t)$	[mL/min]	experimental aqueous phase injection rate
$Q_q^{eff}(t)$	[mL/min]	experimental aqueous phase effluent rate
$X^*_{CO_2\,q}$	[−]	equilibrium CO_2 mole fraction in aqueous phase
$X^{inj}_{CO_2\,q}$	[−]	injected aqueous phase CO_2 mole fraction
Λ	[−]	gas phase effects on oil phase mobility multiplier
$\sigma_{p1,p2}$	[N/m]	surface tension between phases, p1 and p2
d_p	[m]	particle diameter of porous media
S_g^{nuc}	[−]	minimum gas saturation to initiate nucleation
S_{nrc}	[−]	Critical oil saturation during SWI
$\beta_0, \beta_1, \beta_{2\,g}, \beta_{2\,q}, \beta_3, \beta_4$	[−]	non-equilibrium (kinetic) mass transfer coefficients
P^{ref}	[kPa]	reference pressure
T^{ref}	[°K]	reference temperature
a_{wgq}	[kPa]	equilibrium partitioning of water between gas and aqueous phases
$a_{CO_2\,gq}$	[kPa]	equilibrium partitioning of CO_2 between gas and aqueous phases

Chapter 1

1. Introduction and Objectives

1.1 Introduction

Gas saturation can develop in-situ within initially water-saturated porous media after the injection of an aqueous phase that is equilibrated with gas at a pressure higher than the subsurface pressure. During this process, hereafter referred to as supersaturated water injection (SWI), departure from thermodynamic equilibrium (supersaturation of the aqueous phase) leads to the activation of nucleation sites on the solid surface and the appearance of gas bubbles. Continual transport of solute from the bulk aqueous phase to the gas-liquid interfaces leads to gas phase growth, which at the pore-scale leads to the pressurization of bubbles confined in pores by capillary forces and their subsequent expansion into adjacent water-filled pores. A ramified pattern of gas-occupied pores (gas clusters) develops under the influence of capillarity and buoyancy. Gas cluster coalescence during growth, mobilization of sufficiently large clusters under the action of buoyancy, and subsequent fragmentation resulting from capillary instabilities also contribute to the complexity of this process, which was studied by pore network simulation in the first part of this contribution [1]. The simulations suggest that a region of finite extent, where gas exsolution takes place, is established with time in the vicinity of the injection point. Mass transfer from the aqueous to the gas phase is confined in this region, the outer boundaries of which are characterized by dissolved gas concentrations at near-equilibrium levels with the gas phase. Continuous generation of gas within this region drives immiscible displacement and outward propagation of the gas phase. Pore network simulations [1] indicate that advection of the gas phase takes place via a repeated sequence of gas cluster mobilization, fragmentation and coalescence events governed by the interplay of capillary and buoyancy forces. The two-phase flow regime established at steady state is thus likely one of “large ganglion dynamics” rather than “connected pathway flow” [2, 3].

Interest in SWI is motivated by the need to improve the delivery of a gas phase to subsurface environments contaminated by non-aqueous phase liquids (NAPL). Delivery of a gas phase below the water table is needed in bioremediation applications, where oxygen or other reactive gases must be supplied to sustain the destruction of dissolved organic contaminants by micro-organisms [4]. In other instances where contaminants are present as NAPL ganglia trapped below the water table, volatilization

into a flowing gas phase may be an effective remedial strategy [5, 6]. To achieve these goals, *in-situ* air sparging (IAS) has been used to date with varying success [7]. Mass transport effectiveness obviously depends on the spatial distribution of air that can be achieved by IAS within a saturated aquifer. For this reason, a large number of studies have sought to observe and explain the patterns of gas flow during gas injection [8, 9, 10, 11, 12, 13, 14-17]. At the pore scale, variations in air entry pressure due to the ubiquitous random disorder of the pore structure govern the migration of the injected air. During IAS, buoyancy and a highly unfavorable viscosity ratio both have a destabilizing effect on the displacement front which results in the migration of air away from the injection point in the form of separate continuous channels. This picture cannot be accommodated by continuum models of multiphase flow [8, 11, 14, 17] which are consequently limited in their ability to predict air sparging performance in terms of mass transfer.

Bypassing of large portions of the target remediation area due to channeling of the injected air can greatly compromise the remediation effectiveness of IAS. For SWI, on the other hand, one might expect the gas saturation distribution to be relatively insensitive to random disorder of pore size and permeability, at least within the region where gas exsolution takes place. Such an expectation arises from the fact that nucleation can take place in pores of all sizes and the necessary condition for gas cluster growth is transfer of solute mass from the flowing aqueous phase. Gas cluster growth is initially more rapid in areas where the aqueous phase flow velocity is greater, i.e. in more permeable regions within the porous medium. At the same time, an increase of the gas saturation causes reduction of the effective permeability of these areas. Thus, a greater amount of the injected aqueous phase is diverted to less permeable areas, where gas saturation can also develop, as long as the flowing aqueous phase contains sufficient amount of dissolved gas for activation of nucleation sites and sustained mass transfer. Beyond the region where gas exsolution takes place, increasing gas saturation occurs as a result of immiscible displacement. At this scale, gas phase mobility is difficult to ascertain by pore network modeling [1] and a macroscopic (continuum) description of SWI becomes necessary.

Recently, the SWI technology has been show to mobilize non-volatile NAPL ganglia trapped below the water table [18]. Since the mobilization of oil in the subsurface is not clearly understood experiments were conducted to characterize the mechanisms that make an otherwise immobile phase mobile. Short-term and long-term experiments were conducted to determine the effects of three mobile phases in unconsolidated porous media. Short-term experiments provide detailed data collection during the development of gas saturation throughout the column and the resulting aqueous phase effluent. Long-

term experiments focus on the mobilization of oil and the overall oil recovery that can be achieved with three mobile phases.

1.2 Project Objectives

The objective of this project is to measure the dynamics of gas exsolution and flow, as well as oil recovery and flow, observed in long columns, packed with silica sand or glass beads under different conditions (grain size, flow rate and dissolved gas concentration of the injected aqueous phase) of SWI with CO_2 as the dissolved gas. The experimental observations are interpreted using a multiphase, compositional continuum model (CompFlow-SWI) based on the following hypotheses.

- The first hypothesis is that non-equilibrium mass transfer of CO_2 between the aqueous and gas phases can be described by the correlation of Nambi and Powers [19] modified to capture nucleation within the context of continuum modeling. This hypothesis logically follows from pore network simulation results [1].
- A second hypothesis is that gas advection is stabilized by mass transfer so that displacement of the aqueous phase by gas is compact at the macroscopic scale and can, therefore, be described by a continuum model using relative permeability concepts. Specifically, a test is conducted to determine whether the model-predicted advection of the leading edge of the gas phase at a critical saturation is consistent with experimental data.
- The third hypothesis is that the mobility of a disconnected oil phase in the form of ganglia can be predicted using continuum-scale concepts such as relative permeability.
- A fourth hypothesis is that a more accurate oil phase relative permeability function than Stone's Method can be produced for predicting 3-phase systems.

Specifically, the effects of mobile aqueous and gas phases are determined on a previously non-mobile oil phase trapped in the form of ganglia in unconsolidated porous media. SWI experiments aim to understand how aqueous and gas phases interact when mobile and extend this understanding to an oil phase. Initially, Stone's Method was used to determine the oil phase relative permeability in 3-phase systems. However, Stone's Method was found to be inadequate and a new function was developed and calibrated in order to predict oil mobility during SWI in 3-phase systems.

Chapter 2

2. Numerical Model

2.1 Theory

The derivation of the numerical model in this section is based on the idea of using a continuum-based multi-phase compositional approach to describe two processes that are postulated to be central to the description of SWI in porous media. The first process is non-equilibrium (kinetic) transfer of CO_2 between the gas and aqueous phases. It should be noted that such an approach does not simulate the genesis and fate of the gas phase at the pore scale in terms of individual bubbles or distinct clusters of gas-occupied pores, but rather in terms of local gas saturation averaged over a macroscopic volume of the medium containing a multitude of pores. On the basis of experimental data pertaining to the dissolution of residual NAPL in granular media, Nambi and Powers [19] have developed a mass transfer correlation that is valid over a broad range of non-wetting phase saturations. Pore network simulations detailed in the first part of this work [1] suggest that the Nambi and Powers [19] correlation can also be used to describe CO_2 mass transfer between the gas and aqueous phases during SWI. However, this mass transfer correlation does not describe the kinetics of the initial stages of gas phase nucleation [20]. An *ad hoc* modification to the mass transfer correlation is used to account for the rapid increase of gas saturation during nucleation.

The second process involves gas-aqueous-oil 3-phase flow at the continuum scale, where sustained gas flow occurs by mass transfer from an injected aqueous phase rather than direct gas injection. In the context of a continuum-level description, it is hypothesized that gas phase mobility can be described in terms of a saturation-dependent gas relative permeability function and that the multiphase extension of Darcy's law suffices to describe the advective gas flux. A well-known consequence of this hypothesis for one-dimensional displacement in homogeneous porous media is advection of the gas phase as a "shock front", in which its rate of advection is controlled by its relative permeability at a characteristic value of gas phase saturation (greater than the residual gas phase saturation) in a manner analogous to that predicted by the Buckley-Leverett equation [2]. It is also hypothesized that disconnected oil ganglia can be mobilized in porous media by introducing mobile gas and aqueous phases. Experimental evidence suggests that during the "shock front" development, a measureable volume of oil is mobilized and

removed from the system. It is a key objective of this project to evaluate whether these hypotheses conform to experimental observations.

2.2 Assumptions and Boundary Conditions

For the purpose of this thesis assumptions were introduced in order to reduce the complexity of modeling the system.

- Viscosities are assumed to be temperature independent. This does not affect the model predictions because experimental conditions are always around 298K despite vapourization occurring inside of the column. Viscosity is somewhat temperature independent unless large temperature swings are incurred, which makes this a valid assumption.
- Equilibrium partitioning is assumed for the components air, water and oil for aqueous, gas and NAPL phases. Carbon dioxide is the only component that undergoes non-equilibrium partitioning as described by Nambi and Powers (equation 6).
- Pore sizes throughout the column are assumed to be constant. The column is always packed with media that is considered homogeneous, which simply means that the particle sizes are bound within a tight tolerance. If homogeneneity was not assumed for the column a cross-sectional distribution of pore sizes would have to be statistically created for each node, which would only further complicate the process and not significantly change prediction results.
- One difficulty when dealing with gas flow through porous media is the concept of gas compressibility. The model can account for compressibility, pressure and volume changes during transient and steady-state periods. Gas saturations are solely volume-based and a volumetric displacement of the aqueous phase is a sufficient measure during the transient period. However, the pseudo steady-state assumption in the 2-phase experiments is a time when, by definition, there can be no further gas accumulation in the column. Although excess aqueous phase is not observed in the effluent, gas compressibility could allow for gas-density changes throughout this steady-state period. A gas density change would not cause a problem with column saturation, but it may impact gas phase relative permeability if severe enough. It is assumed the gas-density does not change significantly enough to affect flow.
- Unlike the aqueous phase, there is no previous experimental information to characterize gas phase relative permeability (k_{rg}) in a mass-transfer controlled system. Gas phase flow during SWI was observed to be compact unlike similar experiments conducted with air sparging. Gas phase flow during SWI is assumed to follow a Corey curve with an irreducible saturation (S_{gr})

and a Corey constant (n_g). With knowledge of all other component and phase properties in the 2-phase system, it is assumed a Corey curve can be fitted to produce a predictive model.

- The displayed experiments in Chapter 3 and Chapter 4 were chosen because they contain the most relevant and representative data set. All information and figures are available for each experiment for which data has been presented in Chapter 3 and Chapter 4.

The boundary conditions for the fit and predictions of Chapter 3 and Chapter 4 can be found in Figure 1.

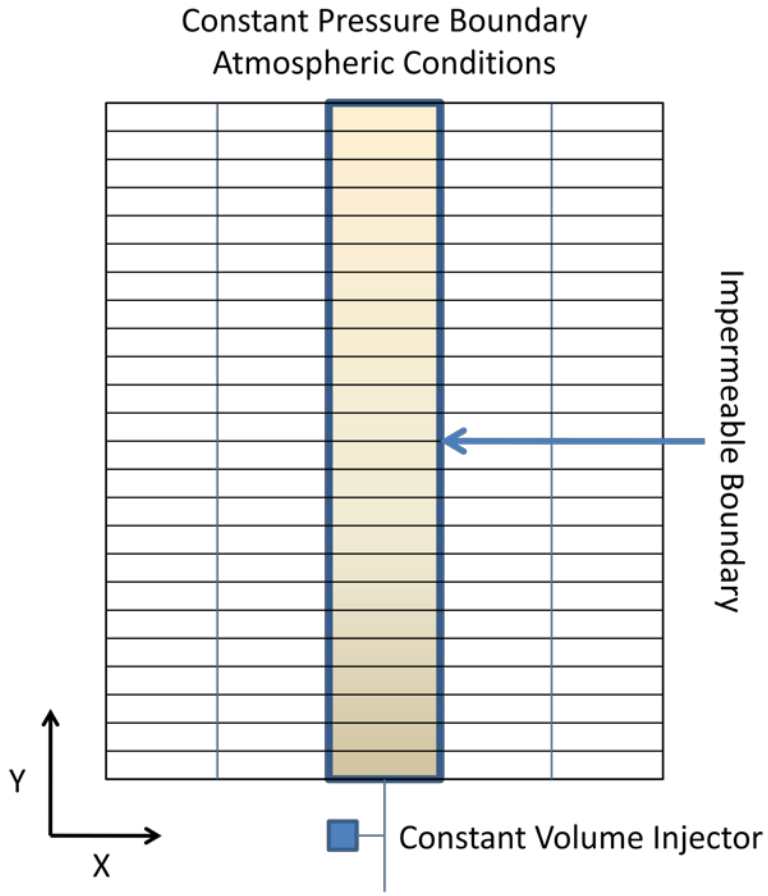

Figure 1 – Boundary conditions for simulations 1-16.

Initial conditions for each column experiment include aqueous, gas and oil saturations and no flowing phase with a hydrostatic pressure gradient. For the experiments contained in Chapter 3 the initial conditions consist of a water-saturated column with no gas or oil phase present. Chapter 4 experiments consist of water-flood residual initial oil saturation, as defined in tables therein, under water-wetted conditions with no gas phase present.

2.3 Formulation

Formulation of the numerical model CompFlow-SWI largely follows that of Forsyth [21]. However, the description of the numerical model is restricted to focus only on those processes relevant to simulating the SWI experiments described here. Specifically, CompFlow-SWI is a continuum-scale multi-phase, multi-component compositional model that considers three mobile phases - the aqueous (q), non-aqeuous (n), and gas (g) phases. The components considered are water (w), air (a), oil (o), and carbon dioxide (CO_2). The conservation of moles of component p can be written as follows. It is important to note that the water and air relationships were combined due to the assumption of equilibrium partitioning throughout the simulation. Each equation (1-4) comprises an accumulation term, a component balance and a molecular diffusion term for each phase. Carbon dioxide also has a generation term which is observed as the rate of non-equilibrium partitioning.

water: $p = \{w\}$

$$\frac{\partial}{\partial t}\sum_{l=q,g}\phi S_l M_l X_{wl} = -\sum_{l=q,g}\nabla\cdot(M_l X_{wl}\mathbf{V}_l) + \sum_{l=q,g}\nabla\cdot(\phi S_l \mathbf{D}_{wl} M_l\,\nabla X_{wl}) + Q_w \tag{1}$$

air: $p = \{a\}$

$$\frac{\partial}{\partial t}\left(\phi S_g M_g X_{ag}\right) = -\nabla\cdot\left(M_g X_{ag}\mathbf{V}_g\right) + \nabla\cdot\left(\phi S_g \mathbf{D}_{ag} M_g\,\nabla X_{ag}\right) + Q_a \tag{2}$$

carbon dioxide: $p = \{CO_2\}$

$$\begin{aligned}\frac{\partial}{\partial t}\left(\phi S_q M_q X_{CO_2\,q}\right) &= -\nabla\cdot\left(M_q X_{CO_2\,q}\mathbf{V}_q\right) + \nabla\cdot\left(\phi S_q \mathbf{D}_{CO_2\,q} M_q\,\nabla X_{CO_2\,q}\right) + \dot{R}_{CO_2} + Q_{CO_2}\\ \frac{\partial}{\partial t}\left(\phi S_g M_g X_{CO_2\,g}\right) &= -\nabla\cdot\left(M_g X_{CO_2\,g}\mathbf{V}_g\right) + \nabla\cdot\left(\phi S_g \mathbf{D}_{CO_2\,g} M_g\,\nabla X_{CO_2\,g}\right) - \dot{R}_{CO_2}\end{aligned} \tag{3}$$

oil: $p = \{o\}$

$$\frac{\partial}{\partial t}\left(\phi[S_q M_q X_{oq} + S_n M_n\right) = -\nabla\cdot\left(M_q X_{oq}\mathbf{V}_q\right) - \nabla\cdot(M_n\mathbf{V}_n) + \nabla\cdot\left(\phi S_q \mathbf{D}_{oq} M_q\,\nabla X_{oq}\right) \tag{4}$$

where Q_p is the rate at which component p is injected/removed (+ve/-ve). By including Q_p in equations 1-4 it is implied that distributed sources/sinks are possible; however, for the purpose of this study only

point source/sink were used and are defined by system boundary conditions. Property data for each phase can be found in Table 1.

In Eq. (3), $\dot{R}_{CO_2}$ represents the non-equilibrium partitioning rate for the exsolution of carbon dioxide from the aqueous to the gas phase, and is given by:

$$\dot{R}_{CO_2} = S_q^{\beta_{2,q}} M_q \kappa_{CO_2} \left(X^*_{CO_2\, q} - X_{CO_2\, q} \right) \tag{5}$$

where $X^*_{CO_2\, q}$ is the mole fraction of carbon dioxide in the aqueous phase in equilibrium with the gas phase. The rate coefficient κ_{CO_2} is adapted from Nambi and Powers [19] and Unger et al. [22] as equation 6:

$$\kappa_{CO_2} = \beta_0 \left[\max\left(S_g,\, S_g^{nuc}\right) \right]^{\beta_{2,g}} \left(\beta_3 + R_q^{\beta_1} \right) \phi^{\beta_4} \frac{D_{CO_2\, q}}{d_p^2} \tag{6}$$

The rate coefficient κ_{CO_2} is a dynamic mass transfer coefficient correlation that was developed and verified in a controlled laboratory experiment. The experiment related the effects of pore size, pore velocity, saturation, and other characteristics to the overall rate of mass transfer through statistical methods described in Nambi and Powers [19]. Although this study determined NAPL dissolution rates into an aqueous phase, it is a close analogy to the non-equilibrium mass transfer experienced during exsolution of a supersaturated gas from an aqueous phase.

A gas saturation, S_g^{nuc}, is introduced *ad hoc* to prevent the computation of unrealistically small mass transfer rates during the initial stages of gas phase formation when $S_g < S_g^{nuc}$, $R_q = \left|v_q\right| \rho_q d_p / \mu_q$ is the aqueous phase Reynolds number, $\left|v_q\right|$ is the magnitude of the interstitial aqueous phase velocity and ρ_q is the mass density of the aqueous phase. The various parameters entering Eq. (6) are summarized in Table 2.

The Darcy flux of each phase l is given by:

$$\mathbf{V}_l = -\mathbf{K} \cdot \frac{k_{rl}}{\mu_l} \nabla (P_l + \rho_l g z) \tag{7}$$

and the dispersion/diffusion tensors have the form:

$$\phi S_l \mathbf{D}_l = \alpha_T^l \mathbf{V}_l \mathbf{I} + \left(\alpha_L^l - \alpha_T^l \right) \frac{\mathbf{V}_l \mathbf{V}_l}{\mathbf{V}_l} + \phi S_l \tau D_{pl} \mathbf{I} \tag{8}$$

The following constraints exist for some of the above variables:

$$S_q + S_g + S_n = 1 \tag{9}$$

$$X_{wq} + X_{CO_2\,q} + X_{oq} = 1 \text{ and } X_{wg} + X_{ag} + X_{CO_2\,g} = 1 \tag{9a}$$

$$P_g = P_n - \alpha P_{cgn}(S_g) + (1-\alpha)[P_{cgq}(S_g) - P_{cnq}(S_q = 1)] \tag{9b}$$

$$P_n = P_q + \alpha P_{cnq}(S_q) + (1-\alpha)P_{cnq}(S_q = 1) \tag{9c}$$

$$\alpha = \min(1, S_n/S_n^*) \tag{9d}$$

where P_{cgq} is the capillary pressure between the gas and aqueous phases; P_{cnq} is the capillary pressure between the water and oil phases; and P_{cgn} is the capillary pressure between the gas and oil phases. The relationships from equations 9-9d are delineated in Forsythe [18] where experimental justification is provided. In essence, the available 2-phase capillary pressure data were combined using saturation information as well as constant multipliers in order to produce 3-phase capillary pressure curves.

Aqueous-gas phase capillary pressure data, P_{cgq}, which for drainage in unconsolidated packs of glass beads and silica sand were taken from the experimental studies of Ioannidis et al. [12] and Leverett [23] respectively, and are plotted in Figure 2 in terms of the Leverett J-function $J(S_q)$: note that each capillary pressure is dependent on its corresponding saturation.

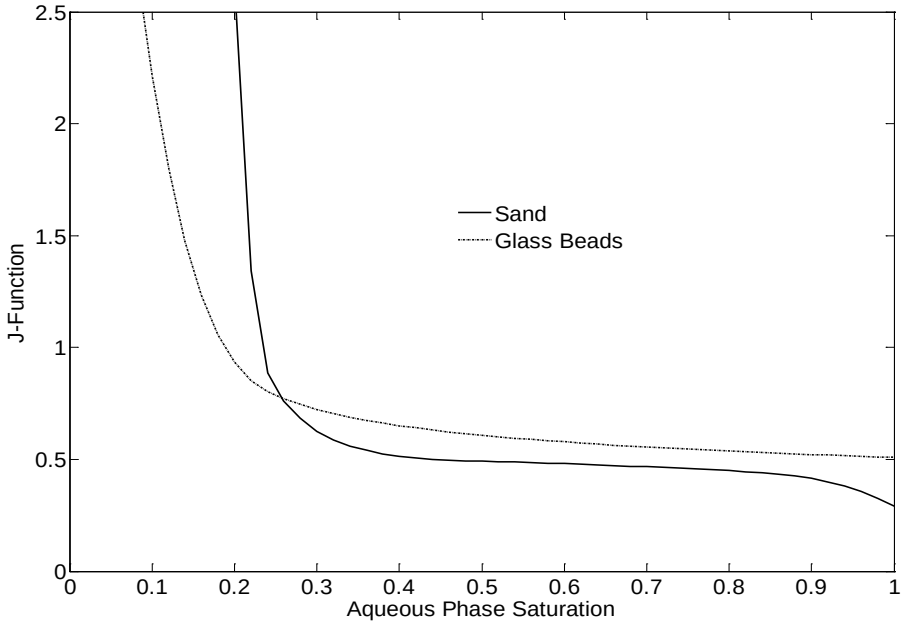

Figure 2 - J-function for air-water drainage in homogeneous packs of sand and glass beads.

$$J(S_q) = \frac{P_{cgq}\left(\frac{\boldsymbol{K}}{\phi}\right)^{0.5}}{\sigma_{gq}} \tag{10}$$

The Leverett J-function is a dimensionless function of water saturation describing a capillary pressure curve [23]. The interfacial tensions were taken to be 26×10^{-3}, 48×10^{-3} and 72×10^{-3} N/m^2 for gas-oil, oil-water and gas-water interfaces respectively. Porosity, absolute permeability, capillary pressure and interfacial surface tensions can be determined from the column setup or independent of experiment.

Equilibrium partitioning of components between the aqueous and gas phases occurs according to the following relationships:

$$X_{wg} = \frac{a_{wgq}}{P_g} X_{wq}$$
$$X_{CO_2\, g} = \frac{a_{CO_2\, gq}}{P_g} X^*_{CO_2\, q} \tag{11}$$

With the air component being insoluble in water, $X_{aq} = 0$. This assumption follows from [21] and allows the gas phase to be present to at least some minimal saturation $S_g^{min} = 10^{-3} \ll S_g^{nuc}$, to alleviate numerical issues associated with the non-condensable air component. Phase and component properties pertinent to the experiments described in this work are listed in Table 2. On the basis of literature values [20], a longitudinal dispersivity α_L^q= 0.1 m was considered representative of all packs in this work with $\alpha_T^q = \alpha_L^g = \alpha_T^g = 0$.

Time derivatives in Eqs. (1-4) are discretized using finite differences with fully-implicit time weighting. A finite volume discretization in one-, two- or three-dimensions is used to handle the spatial derivatives. Details of the discretization can be found elsewhere [18, 21] and will not be repeated here. All of the component equations are fully-coupled and full Newton-Raphson iteration is used for linearization. This yields a large sparse Jacobian matrix which is subsequently solved using ILU factorization and either CGSTAB or GMRES acceleration [24, 25, 26].

Table 1: Component and phase property data (at 20^{o}C).

Property	Value	Source
Compressibility		
$\hat{C}_q$ $[\mathrm{kPa}^{-1}]$	3.0×10^{-6}	[27]
Standard component densities		
M_w^* $[\mathrm{mole/m}^3]$	5.5×10^{4}	[27]
M_a^* $[\mathrm{mole/m}^3]$	41.1	[27]
$M_{CO_2}^*$ $[\mathrm{mole/m}^3]$	41.1	[27]
M_o^* $[\mathrm{mole/m}^3]$	5.13×10^{3}	[27]
Molecular weights		
ω_w $[\mathrm{kg/mole}]$	18.02×10^{-3}	[28]
ω_a $[\mathrm{kg/mole}]$	28.97×10^{-3}	[28]
ω_{CO_2} $[\mathrm{kg/mole}]$	16.0×10^{-3}	[28]
ω_o $[\mathrm{kg/mole}]$	156.0×10^{-3}	[28]
Reference pressure and temperature		
P^{ref} $[\mathrm{kPa}]$	100.0	
T^{ref} $[^{\circ}\mathrm{K}]$	298.0	
Viscosities		
μ_q $[\mathrm{kPa}\cdot\mathrm{day}]$	2.44×10^{-11}	[28]
μ_g $[\mathrm{kPa}\cdot\mathrm{day}]$	1.62×10^{-13}	[28]
μ_n $[\mathrm{kPa}\cdot\mathrm{day}]$	2.64×10^{-11}	[28]
Molecular diffusion coefficient		
$D_{wq} = D_{CO_2q}$ $[\mathrm{m}^2/\mathrm{day}]$	3.14×10^{-6}	[29]
$D_{wg} = D_{ag} = D_{CO_2g}$ $[\mathrm{m}^2/\mathrm{day}]$	1.70×10^{-6}	[29]
Molar density		
$M_q = \dfrac{1+\hat{C}_q\left(P_q - P^{\mathrm{ref}}\right)}{\sum_p \max\left(0, X_{pq}\right)/M_p^*}$, $M_g = \dfrac{P_g}{RT}$		

Table 1 – Continued

Property	Value	Source
Mass density		
	$\rho_l = \sum_p X_{pl}\omega_p$	
Equilibrium partitioning coefficients		
a_{wgq} [kPa]	11.96	[30]
$a_{CO_2\,gq}$ [kPa]	1.651×10^5	[30]
a_{ong} [kPa]	0	Assumption
Interfacial tensions		
σ_{gq} [N/m]	72×10^{-3}	[30]
σ_{nq} [N/m]	48×10^{-3}	[30]
σ_{gn} [N/m]	26×10^{-3}	[30]

Table 2: Simulation parameters and their origin.

Property	Value	Source
Aqueous phase relative permeability in sand		
S_{qr} $[-]$	0.085	[23]
n_q $[-]$	2.21	[23]
Aqueous phase relative permeability in glass beads		
S_{qr} $[-]$	0.20	[12]
n_q $[-]$	2.89	[12]
2- phase gas relative permeability in sand and glass beads		
S_{gr} $[-]$	0.12	this study
n_g $[-]$	1.50	this study
3-phase gas relative permeability in sand and glass beads		
S_{gr} $[-]$	0.18	this study
n_g $[-]$	1.50	this study
3-phase oil relative permeability in sand and glass beads		
S_{nrc} $[-]$	0.06	this study
n_n $[-]$	1.50	this study
Mass transfer rate parameters		
S_g^{nuc} $[-]$	0.03	this study
β_0 $[-]$	37.2	[19]
β_1 $[-]$	0.61	[19]
$\beta_{2\,g}$ $[-]$	1.24	[19]
$\beta_{2\,q}$ $[-]$	0.00	[19]
β_3 $[-]$	0.01	[22]
β_4 $[-]$	1.00	[19]

Chapter 3

3. Gas Exsolution and Flow during Supersaturated Water Injection in Porous Media: Column Experiments and Continuum Modeling

3.1 Experimental Methods and Supplemental Formulation

3.1.1 Experimental Methods

A series of laboratory experiments was conducted in which an aqueous phase supersaturated with CO_2 was injected at the bottom of a vertically-oriented packed column that was initially saturated with degassed water. The solution is supersaturated in the sense that the concentration of CO_2 in the injected aqueous phase is greater than its solubility in water at the column pressure. In order to achieve a supersaturated aqueous phase, tap water and CO_2 gas from a pressurized cylinder were continuously supplied to a hollow-fiber membrane contactor (InVentures Technologies), operating at a pressure of *ca.* 5 atm. The membrane contactor operates by maximizing the exposed surface area of aqueous phase to a dissolvable gas phase at a calibrated pressure. The gas phase pressure is set slightly higher than the liquid phase pressure and this condition is maintained with a controller. The gas phase pushes into the hollow fibers creating a large gas-liquid interfacial surface area which allows for gas to more rapidly dissolve into the aqueous phase.

Figure 3 depicts the experimental setup. A known volume of degassed water was initially added to a Plexiglas column, which is 155 cm long and has an internal diameter of 76 mm. Enough space was allowed for solid silica sand or glass beads to be subsequently packed. Solids were continuously added and wet-packed under vibration or mechanical mixing to prevent the trapping of gas bubbles and to reduce the possibility of layering. Some layering was occasionally observed during this. To prevent the loss of solid particles, fine screens were placed at the top and bottom of the column and supported by springs as necessary.

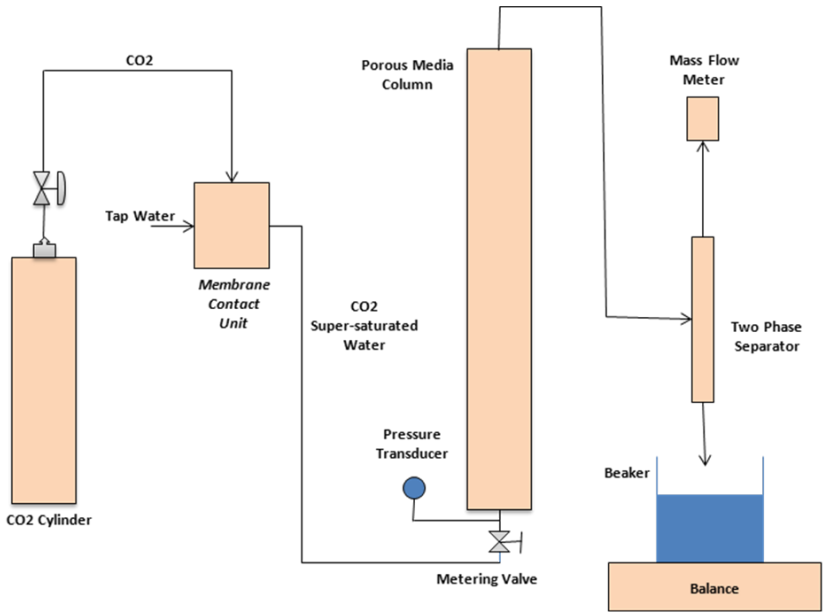

Figure 3 – Experimental setup.

Plates were bolted to the top and bottom of the column to create a closed system with an injection port at the base and sampling ports over the length and at the top of the column. The porosity of the packing was determined from knowledge of the column dimensions, mass of solids added, and the volume of water displaced by the solids added. Finally, the absolute permeability of the packing was determined by measuring the water flow rate under a fixed pressure gradient. Table 1 summarizes the porous media properties for nine experiments forming the basis of this work. The ratio of buoyant to capillary forces in these systems is also quantified in Table 1 in terms of the Bond number, defined as follows:

$$Bo = \frac{\left(\rho_q - \rho_g\right) g \, \mathbf{K}}{\sigma_{gq}} \tag{12}$$

where ρ_q and ρ_g are the mass density of the aqueous and gas phases, g is gravitational acceleration, $\mathbf{K}$ is the absolute permeability of the system, and σ_{gq} is the interfacial tension between the gas and aqueous phases.

Aqueous and gas phase effluents from the column were sent to a graduated pipette acting as a phase separator. The mass of aqueous phase effluent was collected in a beaker and measured continuously using a digital balance interfaced with a computer. Also interfaced with a computer were a mass flow meter (Omega, model FMA3304) to measure the effluent rate of gas consisting of nearly 100% CO_2, and a pressure transducer (Validyne, model DP10-44) to monitor the aqueous phase pressure at the base of

the column. Aqueous phase samples were drawn from sampling ports at distances of 75 cm and 145 cm from the column base to determine the concentration of dissolved CO_2.

At the start of each experiment the column was either freshly packed and, therefore, completely saturated with degassed water, or flushed with copious amounts of degassed water to ensure that no gas phase from a previous experiment remained entrapped in the porous media. To conduct an experiment, the valve at the bottom was opened at time t_0 and CO_2–supersaturated water was allowed to flow through the column at constant rate until time t_{SWI}, a period of time sufficiently long for the aqueous phase effluent rate to reach a constant steady-state value. At steady-state, the rate of accumulation of gas within the column was zero and a measurement of the aqueous phase effluent rate provided the flow rate of the injected aqueous phase, Q_q^{inj}. The mole fraction of dissolved CO_2 in the injected aqueous phase, $X_{CO_2\,q}^{inj}$, was also determined experimentally as follows because of the inability to precisely control the level of super-saturation entering the system. Despite setting the pressure and flow rates, the saturation unit was not able to produce predictable results. Once an experiment began, the exsolution of carbon dioxide was able to create a consistent gas flow rate but that flow rate could not be determined *a priori*.

Aqueous phase effluent was first drawn from the top sampling port following establishment of a steady aqueous effluent rate. The effluent sample was immediately added to a sodium hydroxide solution of pH greater than 11. The sodium hydroxide was in excess to ensure that all dissolved CO_2 was converted into disodium carbonate. This mixture was then titrated with hydrochloric acid using phenolphthalein as the titration indicator. Initially the solution was translucent, but changed color as the pH was reduced to 11. The titration was complete when the pH dropped below 9 and the solution became translucent once again. At this point, all of the disodium carbonate was converted into sodium bicarbonate and a mole balance was used to determine the original amount and, hence, the mole fraction of CO_2 in the aqueous effluent. The mole fraction of carbon dioxide in the injected aqueous phase, $X_{CO_2\,q}^{inj}$, was then determined from a steady-state mass balance of CO_2 over the entire column using the experimentally measured aqueous and gas phase effluent rates, Q_q^{eff} and Q_g^{eff}. The values of Q_q^{inj} and $X_{CO_2\,q}^{inj}$ for each experiment were determined from steady-state values of Q_q^{eff} and Q_g^{eff} are listed in Table 4.

In each experiment, SWI was stopped at time t_{SWI} and the column response was monitored over time until steady-state was again reached. Experimental data from the two transient periods, one following SWI commencement and the other following SWI termination, are particularly interesting because they

are sensitive indicators of the ability of the continuum model to describe the SWI process. In subsequent sections, these data are discussed separately.

3.1.2 Gas/Aqueous Phase Relative Permeability

Aqueous (k_{rq}) and gas (k_{rg}) phase relative permeability values for both the sand and glass bead packs are represented as follows [31]:

$$k_{rq} = \left(\frac{S_q - S_{qr}}{1 - S_{qr}}\right)^{n_q}$$
$$k_{rg} = \left(\frac{S_g - S_{gr}}{1 - S_{gr}}\right)^{n_g} \quad (13)$$

where S_{qr} and S_{gr} are the residual aqueous and gas phase saturations, respectively. The residual values for each phase describe its irreducible saturation when contained in water-wetted porous media. The gas phase relative permeability parameters S_{gr} and n_g were estimated in this study. Conversely, the aqueous phase relative permeability parameters S_{qr} and n_q for packs of sand and glass beads were taken from the experimental works of Leverett [23] and Ioannidis et al. [12], respectively. All parameter values are summarized in Table 2 and varieties of the relative permeability functions with respect to saturation are plotted in Figure 4.

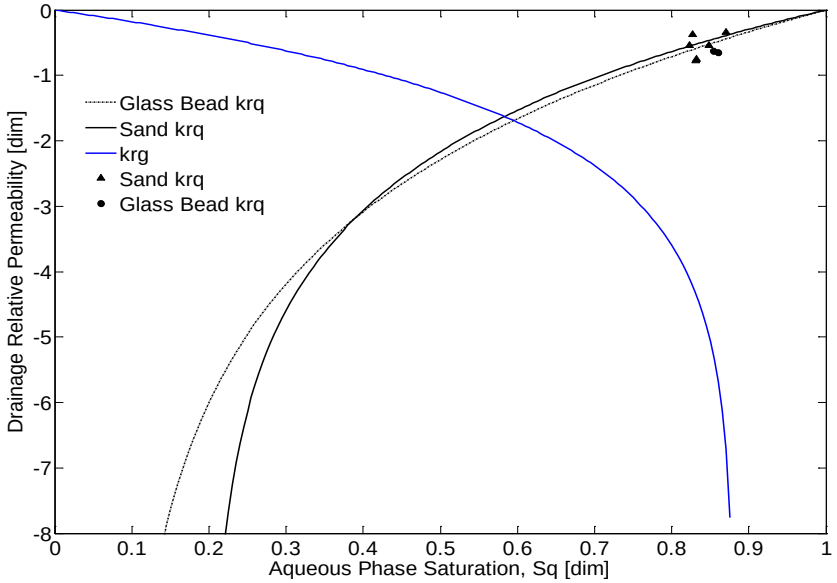

Figure 4 - Aqueous and gas phase relative permeability curves.

The shaded symbols shown in Figure 4 are the experimental steady state aqueous phase relative permeability values for glass bead (circles) and sand pack (triangles) were computed by using the multi-phase extension of the Darcy equation as: $k_{rq}(S_q) = \left(Q_q^{inj}\,\mu_q\,L\right)/\left(\mathbf{K}\,A\,\Delta\Gamma_q\right)$ where L is the column length, A is its cross-sectional area, $\Delta\Gamma_q = P_q(t_{SWI}) - P^{\mathrm{ref}} - \rho_q g L$, and $S_q = 1 - \Delta\bar{S}_g(t_{SWI})$. It should be noted that actual experimental data was used to find these data points. The points are plotted to reaffirm that the Leverett and Ioannidis relative permeability curves are valid during experiment.

Since the gas phase relative permeability has never been measured for flowing gas exsolution in the presence of a flowing aqueous phase, it had to be estimated. The gas phase relative permeability curve was assumed to have the shape of a Corey curve with irreducible gas saturation and a Corey constant. To estimate these values, experiments 1-8 were simulated with a trial and error method. The irreducible saturation and the Corey constant appear to be heavily correlated and only one combination of the two were able to reproduce each experiment. The simulation results are highly sensitive to any change in the irreducible saturation and the Corey constant.

3.2 Results and Discussion

In the simulations reported here, only S_g^{nuc} (see Eq. (6)) and the gas relative permeability parameters S_{gr} and n_g (see Eq. (13)) were considered adjustable. Every other parameter was independently measured or estimated: such as absolute permeability, injection pressure, aqueous phase carbon dioxide content, aqueous phase flow rates, aqueous phase relative permeability curves, and mass transfer interactions. Experimental observations and numerical results are discussed which pertain to the time period $t_0 \le t \le t_{SWI}$ (SWI transient and steady state) from those pertaining to the time period $t_{SWI} < t \le t_{p-SWI}$ (post-SWI transient), all with reference to experiment 8 (see Tables 3 and 4) against which the continuum model is calibrated. Subsequently, it is hypothesized that the remaining experiments can be *predicted* using the same set of parameter values (S_g^{nuc}, S_{gr} , n_g). The post-SWI information affords an additional test on the ability of the continuum model to describe gas exsolution and flow when SWI is stopped, but a driving force for mass transfer remains. This driving force is a consequence of two factors, volumetric expansion of the gas phase as pressures return to hydrostatic and an increase in the level of CO_2 supersaturation of the aqueous phase due to the decline in aqueous phase pressure.

3.2.1 SWI Transient and Steady State Behaviour

Figure 5 shows the experimental (symbols) and simulated (lines) results for experiment 8. The black circle denotes the pore volume relative time that the aqueous phase effluent sample was taken and used to determine $X_{CO_2\,q}^{inj}$ as listed on Table 3.

The aqueous phase effluent increases very rapidly above the expected Q_q^{inj}, during the early time periods where no gas phase effluent is produced. A rapid increase of the injection pressure is also observed as the relative permeability of the aqueous phase is reduced in the presence of gas within the pore space. As soon as SWI is initiated, miscible displacement of the CO_2-free resident aqueous phase by the CO_2-rich injected aqueous phase takes place, resulting in nucleation and growth of the gas phase in the lowest part of the column.

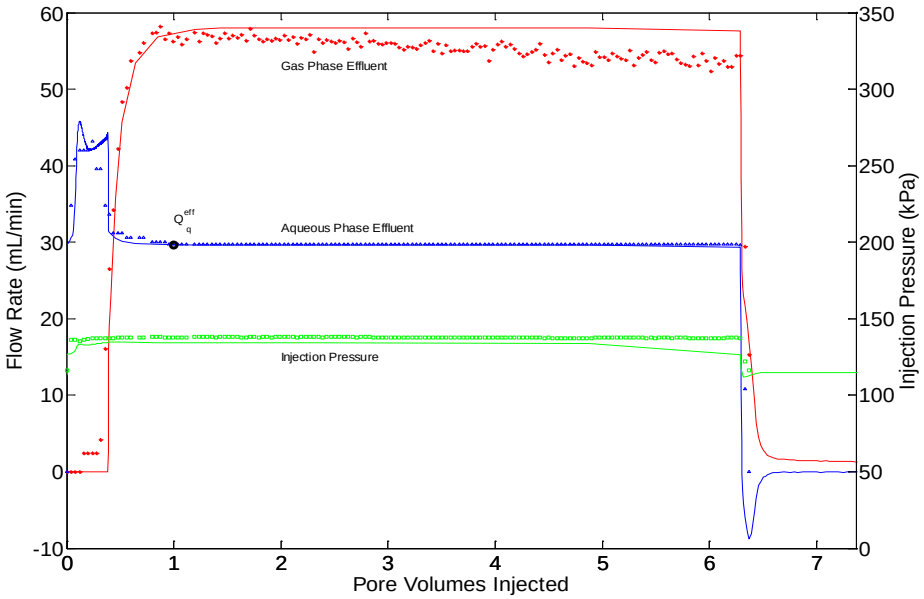

Figure 5: Aqueous and gas phase effluent data and injection pressure data.

As gas saturation develops, a volumetric displacement occurs which is observed as an increase in the aqueous phase effluent rate. The aqueous phase injection rate, Q_q^{inj}, is constant throughout the experiment, which allows for the aqueous phase effluent rate, Q_q^{eff}, to be used as the primary method to calculate the average gas saturation in the column. The total volume of displaced aqueous phase and thus the column-averaged change in gas saturation $\Delta\bar{S}_g$ at time t_{SWI} can be determined as follows:

$$\Delta\bar{S}_g(t_{SWI}) \approx \int_{t_0}^{t_{SWI}} [Q_q^{eff}(t) - Q_q^{inj}]\, dt \tag{14}$$

At the end of the transient period, $Q_q^{eff} = Q_q^{inj}$, and the rate of gas accumulation in the column is zero. It is important to note that gas flow out of the column does not begin until the gas saturation is nearly fully developed. The aqueous phase effluent rate, Q_q^{eff}, remains constant thereafter until SWI is terminated at time t_{SWI}, after injection of about 6 PV of CO_2-supersaturated aqueous phase. On the contrary, the measured gas flow rate which reaches a maximum once a steady gas saturation is established, is observed to decrease gradually with time as a result of a decreasing mole fraction of dissolved CO_2 in the injected aqueous phase, $X_{CO_2\,q}^{inj}$. This is a consequence of unpredictable variability in the performance of the membrane contactor.

No attempt was made to incorporate temporal changes of $X_{CO_2\,q}^{inj}$ in the simulation. Instead, it was assumed that $X_{CO_2\,q}^{inj}$ is constant and equal to the value determined experimentally as explained in Section 3.1.1. The actual aqueous phase sample used to perform this calculation is shown by the large open circle in Figure 5. The simulation accurately reproduces experimental measurements of aqueous phase effluent flow, gas phase effluent flow, and injection pressure throughout the time period $t_0 \leq t \leq t_{SWI}$. Such agreement was achieved using the gas phase relative permeability function plotted in Figure 3 and $S_g^{nuc} = 0.03$ in the mass transfer rate expression, Eq. (6). It was found that unless such an *ad hoc* modification of the mass transfer rate expression is made, the continuum model is unable to accurately describe the dynamics of gas accumulation in the column for any choice of gas phase relative permeability. This is to be expected because the kinetics of the initial stages of gas phase formation (nucleation) [20, 32], which are not explicitly accounted for in the continuum model, are markedly different from the kinetics of non-equilibrium mass transfer between a flowing aqueous phase and non-wetting gas phase ganglia [19].

A more in-depth examination of the experimental observations is possible with the help of the numerical model. Figure 6 shows again measured and predicted aqueous phase effluent during the initial transient period of SWI.

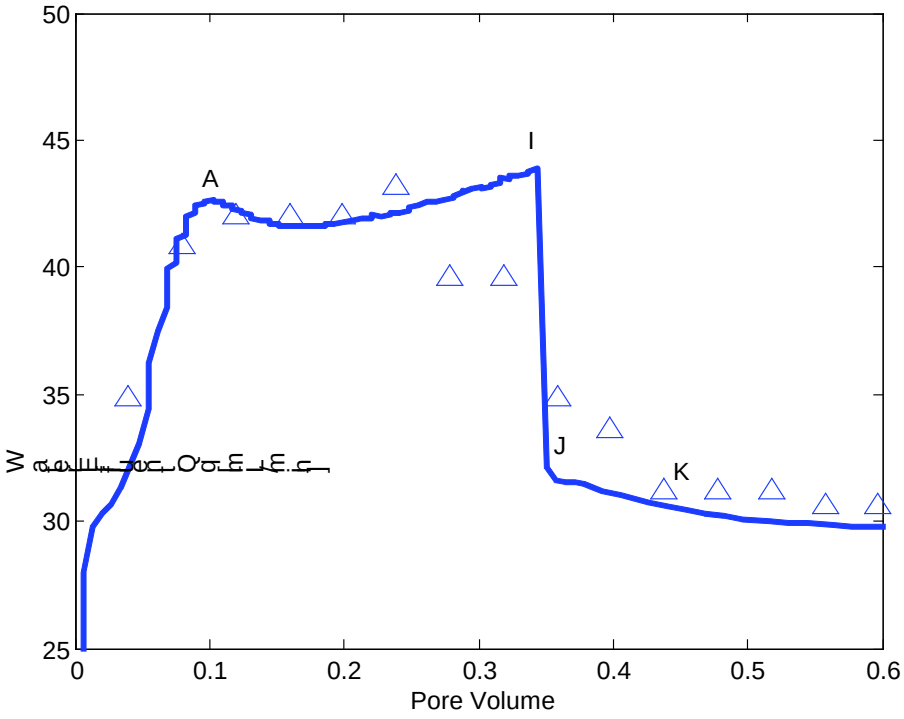

Figure 6: Aqueous phase effluent during gas saturation growth.

The experimental (symbols) and simulated (line) aqueous phase effluent rate during SWI as a function of PV of aqueous phase injected (experiment #8): A = 0.10 PV, I = 0.34 PV and J = 0.36 PV. A number of time points of interest to this transient behavior are identified with letters (A, I, and J) in this figure. These points are discussed with reference to Figure 7, which plots the simulated spatiotemporal evolution of gas phase saturation and CO_2 content of the resident aqueous phase. Figure 6 also presents the mole fraction of dissolved CO_2 at conditions of equilibrium between the gas and aqueous phases, determined from Henry's law (see Eq. (10)) at the prevailing steady-state aqueous phase pressure distribution and temperature $\boldsymbol{T}^{\mathbf{ref}}$.

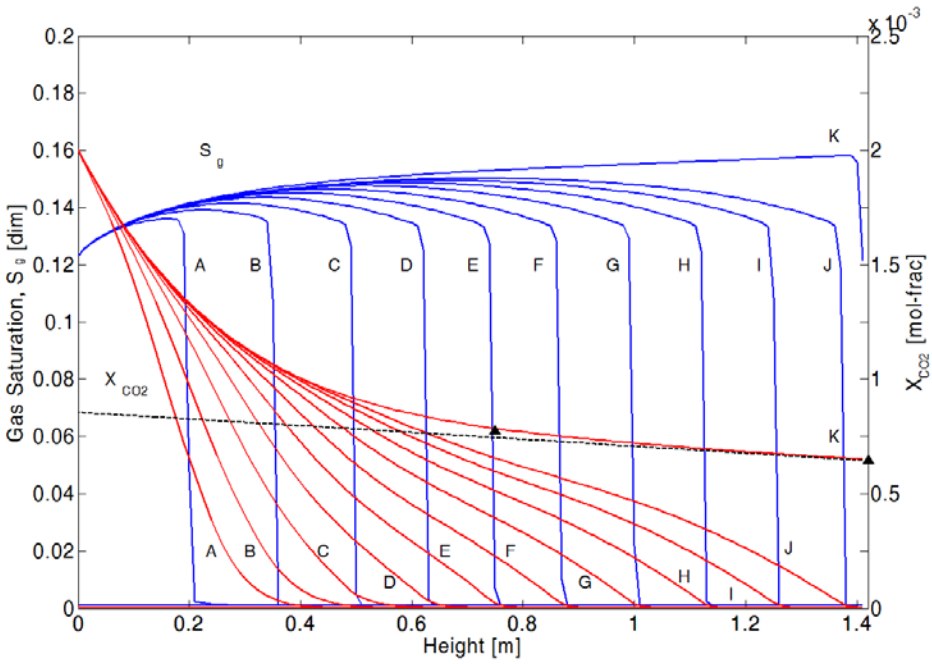

Figure 7: Simulation gas saturation and CO_2 concentration during SWI.

The simulated gas phase saturation (solid blue lines), S_g, and mole fraction of dissolved CO_2 (solid red lines), $X_{CO_2\,q}$, as functions of column height for experiment 8 at different times: A = 0.10 PV, B = 0.13 PV, C = 0.16 PV, D = 0.19 PV, E = 0.22 PV, F = 0.25 PV, G = 0.28 PV, H = 0.30 PV, I = 0.34 PV, and J = 0.36 PV. The dashed line represents the mole fraction of dissolved CO_2 in equilibrium with the gas phase ($X^*_{CO_2\,q}$). Symbols (black filled triangles) represent measurements of aqueous phase CO_2 mole fraction at time $t = t_{SWI}$ (during steady-state SWI).

The difference between the bulk and equilibrium CO_2 concentration in the aqueous phase is the driving force for nucleation and subsequent growth of the gas phase. Therefore, Figure 7 provides insight into: (1) the time evolution of the extent of a macroscopic region in which nucleation and mass transfer-driven *growth* of the gas phase can take place; and (2) the development and propagation of a sharp gas saturation front. With the help of Figure 7, it is straightforward to identify experimental point A in Figure 6 as the point in time when the gas phase has just surpassed the zone where nucleation is possible. Nucleation is possible in any area where gas does not exist and the actual dissolved carbon dioxide is greater than the equilibrium level of dissolved carbon dioxide for a particular height in the column. Thereafter, the gas phase saturation front advances *past* the zone where CO_2-supersaturation of the aqueous phase exists. During the early stages of SWI, for times and positions above point A, the advancing gas saturation front encounters a resident aqueous phase. The encountered aqueous phase

has very low levels of dissolved carbon dioxide, which allows CO_2 from the gas phase to *dissolve* into the aqueous phase, given that the column is initially saturated with an aqueous phase in equilibrium with atmospheric conditions. This is also surmised from Figure 8, which plots directly simulation results for $\dot{R}_{CO_2}$ representing the rate of CO_2 exsolution along the column.

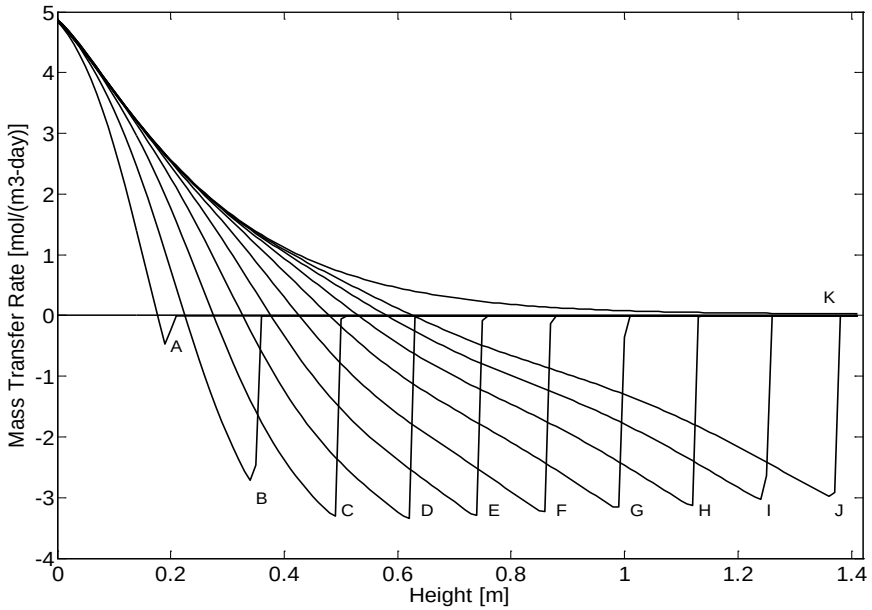

Figure 8: Simulation mass transfer rates during SWI.

The simulated mass transfer rate of carbon dioxide from the aqueous to the gas phase (given by $\dot{R}_{CO_2}$ from Eq. (4)) as a function of column height for experiment 8 at different times: A = 0.10 PV, B = 0.13 PV, C = 0.16 PV, D = 0.19 PV, E = 0.22 PV, F = 0.25 PV, G = 0.28 PV, H = 0.30 PV, I = 0.34 PV, J = 0.36 PV, and steady state (K). Here, the rate of exsolution is shown to take on negative values past point A and until steady state is established, implying mass transfer of CO_2 from the gas to the aqueous phase. Experimental point I in Figure 6 represents the point in time when a sharp reduction in the rate of gas phase accumulation in the column is observed. As shown in Figure 7, the simulated gas phase saturation front is very near the top of the column at this time. Point J in Figure 6 is the point in time when significant gas production is first experimentally observed (see also Figure 5) and agrees with the simulation results shown in Figure 7. Furthermore, Figure 7 shows that the simulated gas phase saturation distribution changes very little after the arrival of the gas saturation front at the top of the column. During this time period, equilibrium partitioning of CO_2 is established at the top part of the column (see Figure 7) as a result of gas phase dissolution (see Figure 8). Aqueous phase samples taken

at steady state from two sampling ports and analyzed for dissolved CO_2 corroborate the numerical model results (see data points shown as triangles in Figure 7). At steady state, an average gas saturation of 0.149 is predicted by the continuum model, which is in excellent agreement with the experimental value of $\Delta\bar{S}_g(t_{SWI}) = 0.145$ as reported on Table 5.

Remarkably, the experimental observations are consistent with a model of compact displacement of the aqueous phase by the exsolved gas. As can be seen in Figure 7, this displacement is described by advancement of a shock front at $S_g \approx 0.135$, a saturation just higher than the value of the residual gas saturation (S_{gr} = 0.12) quantifying the threshold of gas phase mobility. The magnitude of the critical gas saturation, S_{gc}, the saturation associated with the onset of bulk gas flow in pore networks in which gas saturation develops as a result of phase change, has been previously studied by Tsimpanogiannis and Yortsos [33]. In the absence of mass transfer limitations, S_{gc} has been found to be independent of the Bond number, *Bo*, in the low-*Bo* range (*Bo* < 10^{-4}) and coincident with the threshold of percolation processes originating from multiple nucleation centers [33]. A consistent estimate of this threshold saturation for our system is fairly tight, 0.12 < S_{gc}< 0.135. The fact that this estimate is very close to the gas saturation associated with the percolation threshold for drainage of the aqueous phase (see Figure 2) is no surprise considering the low Bond number [33]. With regards to displacement patterns at the macroscopic scale, gas-liquid two-phase flow during SWI is markedly different from gas-liquid flow during IAS, the latter generally characterized by channeling of the injected gas phase [8, 9, 10, 15, 16]. During SWI, the basic premise of a continuum-scale description, namely the existence of a macroscopic representative elementary volume (REV) for gas saturation, is evidently supported by the uniform nature of gas phase exsolution.

The continuum model can describe quantitatively all observations associated with experiment 8, subject only to adjustment of parameters affecting the gas relative permeability (S_{gr} and n_g in Eq. (13)) and mass transfer rate at the initial stage of gas phase formation (S_g^{nuc} in Eq. (6)), as mentioned above. The sensitivity of these parameters to changes of particle size, flow rate and dissolved CO_2 concentration of the injected aqueous phase is, of course, of great interest. Gas phase advection during SWI takes place via a repeated sequence of mobilization, fragmentation and coalescence of large gas clusters [34]. It is hypothesized that the aforementioned parameters would be relatively insensitive to changes of grain size, flow rate and dissolved CO_2 concentration of the injected aqueous phase, as long as the Bond number characterizing different systems is sufficiently small (*Bo* < 10^{-4}). To test this hypothesis, two additional experiments (experiments 7 and 9, see Tables 3 and 4) were simulated in the same glass bead

pack as the one used in experiment 8, and six SWI experiments in uniform sand packs of different permeability (experiments 1-6, see Tables 3 and 4) using the same parameters.

A visual assessment of the ability of the continuum model to *predict* SWI experiment 6 in packed columns is shown in Figure 9. Similar results were obtained for all other experiments and are not shown. In each case, the continuum model provides a reasonable prediction of the gas and water effluent rates and injection pressure.

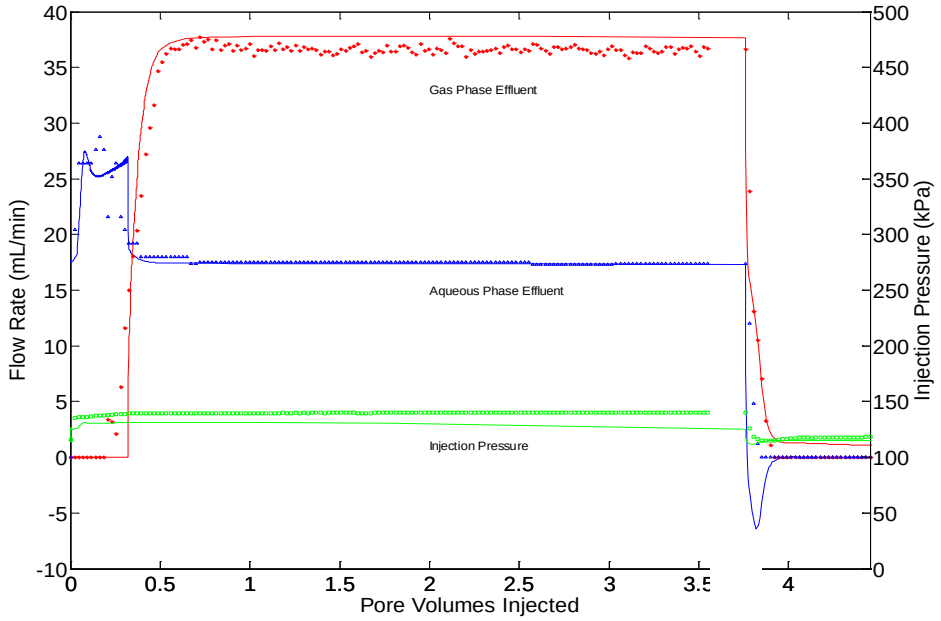

Figure 9: Experimental (symbols) and simulated (lines) results for experiment 6.

A quantitative assessment of the predictive ability of the continuum model is given in Table 5 in terms of the column-average change in gas phase saturation, $\Delta\bar{S}_g$, established in the columns during SWI at steady state as determined by Eq. (14). On average, the simulation underestimates the experimentally observed change of gas saturation at steady state in sand-packed columns by less than 0.02, whereas it is within 0.01 for the column filled with glass beads. In all experiments considered, gas exsolution occurs only in the bottom half of the column. In addition, the aqueous phase effluent is at equilibrium with a pure CO_2 gas phase at P^{ref} which is the pressure at the column outlet. On the basis of these findings, the hypothesis that gas relative permeability during SWI is relatively insensitive to the grain size, injected aqueous phase flow rate and dissolved CO_2 concentration cannot be rejected. Notwithstanding, these parameters were varied within narrow ranges and further testing is necessary.

3.2.2 Post-SWI transient

Without exception, the gas effluent rate is observed to decay very rapidly to zero as soon as injection of the CO_2-supersaturated aqueous phase is stopped (see Figure 5 and Figure 9). The same is true of the aqueous phase effluent rate and relevant experimental data are detailed in Figure 10. Careful consideration of these observations affords us additional insight into the strengths and limitations of the proposed continuum-level description of gas exsolution and flow during SWI.

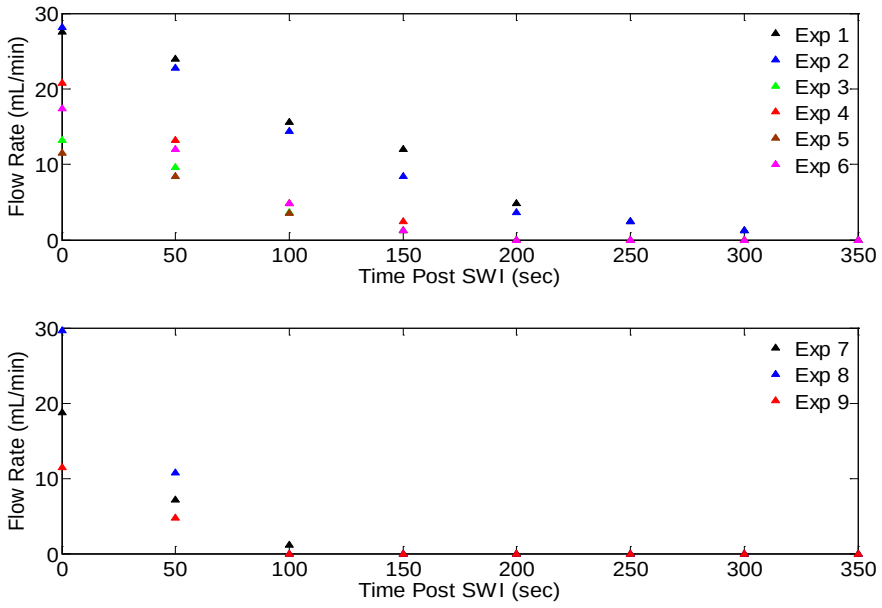

Figure 10: Observed aqueous phase effluent rates for the post-SWI transient

The experimental data, $\boldsymbol{Q_q^{eff}(t)}$ in Eq. (15), for sand and glass bead column experiments. The data indicate that there is further change (increase) of column-average gas saturation, which is given by the following equation:

$$\Delta\bar{S}_g(t_{p-SWI}) \approx \int_{t_{SWI}}^{t_{p-SWI}} Q_q^{eff}(t)\, dt \tag{15}$$

where $t_{SWI} < t \leq t_{p-SWI}$ is the post-SWI observation time period and $\Delta\bar{S}_g(t_{p-SWI})$ represents the change in the column average gas saturation during this time. Once SWI is terminated, the pressure of the column is suddenly reduced to hydrostatic. A first consequence of a reduction in liquid pressure is volumetric expansion of the gas phase and therefore displacement of some of the aqueous phase. This

consequence is accounted for in the continuum model. Other consequences are related to additional gas phase formation (nucleation) and mass transfer-driven growth as explained below.

Both nucleation and mass transfer are processes linked to departure from thermodynamic equilibrium as measured, for example, by the following ratio of CO_2 mole fractions in the aqueous phase:

$$\mathcal{S}_f = \frac{X_{CO_2\,q}}{X^*_{CO_2\,q}} \tag{16}$$

where $X_{CO_2\,q}$ and $X^*_{CO_2\,q}$ represent the actual and equilibrium CO_2 content of the aqueous phase and $\mathcal{S}_f$> 1 denotes supersaturation. The degree of supersaturation varies with location and is highest at the base of the column, where it may be readily estimated from knowledge of the aqueous phase pressure. Assuming that the reduction of the column pressure to hydrostatic (i.e., $P_g(t_{SWI}) \rightarrow P_g\left(t_{p-SWI}\right)$) is instantaneous, the mole fraction of CO_2 in the aqueous phase at the bottom of the column remains unchanged and is equal to $X^{inj}_{CO_2\,q}$. Therefore, the change of $\Delta\mathcal{S}_f$, the degree of supersaturation, is realized by the sudden reduction in the pressure of the aqueous phase as follows:

$$\Delta\mathcal{S}_f = \frac{X^{inj}_{CO_2\,q}}{X^*_{CO_2\,q}|_{P_g(t_{p-SWI})}} - \frac{X^{inj}_{CO_2\,q}}{X^*_{CO_2\,q}|_{P_g(t_{SWI})}} \tag{17}$$

As shown in Table 5, reduction of the aqueous phase pressure to hydrostatic causes an *increase* in the degree of supersaturation at the base of the column. In turn, this implies an increase in the driving force for CO_2 transfer from the aqueous to the gas phase (see Eq. (5)), resulting from a decrease in P_g in Eq. (10), which is accounted for in the continuum model. Another, rather distinct, implication is gas phase formation at a number of nucleation sites not previously activated leading to the appearance of gas phase in pores which at the conclusion of SWI contained only aqueous phase. This implication is consistent with progressive nucleation theory [32], according to which each nucleation site is activated at a different supersaturation threshold. By reducing the column pressure without affecting the aqueous phase carbon dioxide concentration, the supersaturation factor was increased and caused previously inactive nucleation sites to activate. Our *ad hoc* correction to the Nambi and Powers model, S_g^{nuc} , which was found adequate for describing the rapid increase in gas saturation due to nucleation at the initial stage of SWI, has no effect at the post-SWI stage given that the gas phase saturation in the column is above 0.03. Table 5 shows that in every case the simulation *underestimates* the post-SWI gas

saturation growth $\Delta\bar{S}_g$. The underestimation of gas phase saturation appears to follow a pattern closely related to the value of supersaturation in the aqueous phase $\Delta\mathcal{S}_f$, as shown in Figure 11.

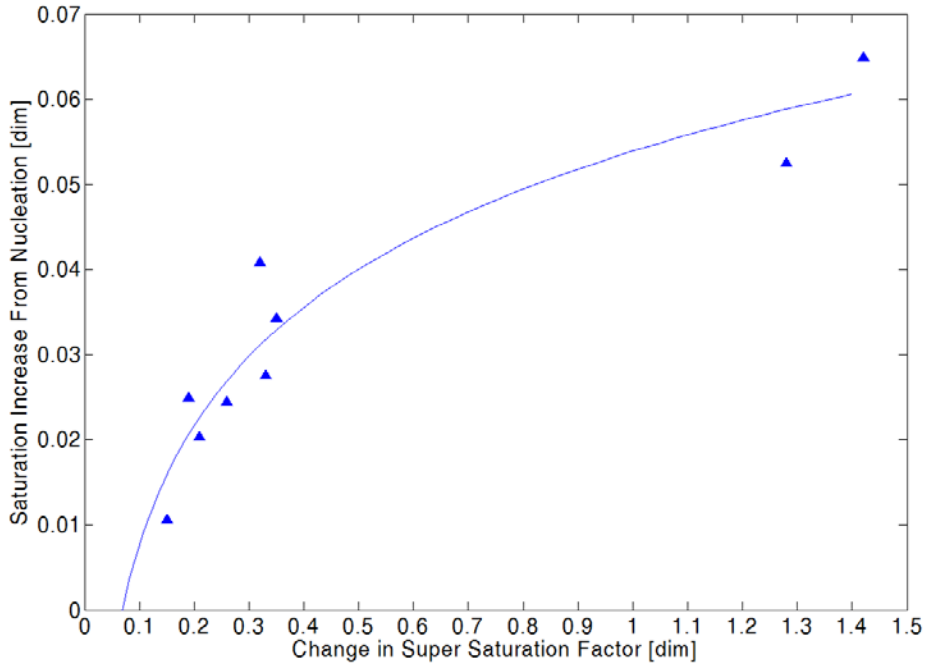

Figure 11: Gas saturation increase during SWI as a function of supersaturation.

The observed increase in gas phase saturation after SWI that is not accounted for in the simulation and is attributed to nucleation. This is quantified as the difference between observed and simulated increase in gas phase saturation $\Delta\bar{S}_g(t_{p-SWI})$ and plotted against the change in the supersaturation factor $\Delta\mathcal{S}_f$ as defined by Eq. (17) and listed on Table 5. The solid line on the figure is only a guide to the eye. This finding is consistent with progressive nucleation theory, which states that nucleation sites can become active if a sufficient supersaturation factor is achieved [32]. It also illustrates a limitation in the way the effects of nucleation are presently handled in the continuum model.

Table 3: Properties of packed columns used in CO_2-SWI experiments.

Experiment ID	Packing	Permeability $K\ [\mathrm{m}^2]$	Average Particle Size $d_p\ [\mu m]$	Porosity $\phi\ [-]$	$Bo\ [-]$
1	Sand	1.12×10^{-11}	169	0.367	$1.52\text{x}10^{-6}$
2	Sand	1.12×10^{-11}	169	0.367	$1.52\text{x}10^{-6}$
3	Sand	2.91×10^{-11}	305	0.350	$3.96\text{x}10^{-6}$
4	Sand	4.05×10^{-11}	324	0.351	$5.51\text{x}10^{-6}$
5	Sand	3.82×10^{-11}	324	0.352	$5.20\text{x}10^{-6}$
6	Sand	3.82×10^{-11}	324	0.352	$5.20\text{x}10^{-6}$
7	Glass beads	5.65×10^{-11}	254	0.384	$7.68\text{x}10^{-6}$
8	Glass beads	5.65×10^{-11}	254	0.384	$7.68\text{x}10^{-6}$
9	Glass beads	5.65×10^{-11}	254	0.384	$7.68\text{x}10^{-6}$

Table 4: Experimental control variables and measurements.

Experiment ID	Control Variables		Measurements		
	Q_q^{inj}	$X_{CO_2\,q}^{inj}$	$P_q(t_{SWI})$	$P_q(t_{p-SWI})$	$Q_g^{eff}(t_{SWI})$
	$[\mathrm{mL/min}]$	$[-]$	$[\mathrm{kPa}]$	$[\mathrm{kPa}]$	$[\mathrm{mL/min}]$
1	27.60	0.002902	188.5	118.6	87.23
2	28.15	0.002599	188.5	118.6	76.14
3	13.20	0.002076	131.7	118.6	26.20
4	20.82	0.002099	133.8	118.6	44.28
5	11.49	0.001798	128.7	118.6	20.16
6	17.40	0.002111	135.8	118.6	37.76
7	18.72	0.001992	128.7	118.6	37.13
8	29.66	0.002005	135.8	118.6	58.16
9	27.60	0.001804	126.7	118.6	20.02

Table 5: Column-average gas phase saturation and inlet aqueous phase CO_2-supersaturation.

Experiment ID	ΔS_f	**observed** $\Delta\overline{S}_g$	**predicted** $\Delta\overline{S}_g$	**prediction error** $\Delta\overline{S}_g$
$t_0 \leq t \leq t_{SWI}$	$t = t_0$	$t = t_{SWI}$	$t = t_{SWI}$	
1	2.42	0.173	0.163	0.010
2	2.16	0.130	0.158	-0.028
3	2.47	0.152	0.150	0.002
4	2.46	0.177	0.154	0.023
5	2.19	0.167	0.144	0.023
6	2.44	0.169	0.152	0.017
7	2.43	0.140	0.146	-0.006
8	2.32	0.145	0.149	-0.003
9	2.24	0.148	0.140	0.008
$t_{SWI} < t \leq t_{p-SWI}$	$t > t_{SWI}$	$t = t_{p-SWI}$	$t = t_{p-SWI}$	
1	1.42	0.104	0.039	0.065
2	1.28	0.094	0.042	0.052
3	0.27	0.031	0.007	0.024
4	0.32	0.045	0.005	0.040
5	0.19	0.028	0.003	0.025
6	0.35	0.040	0.005	0.035
7	0.21	0.024	0.004	0.020
8	0.33	0.034	0.007	0.027
9	0.15	0.013	0.003	0.010

Chapter 4

4. Oil Recovery and Flow during Supersaturated Water Injection in Porous Media: Column Experiments and Continuum Modeling

4.1 Experimental Methods and Supplemental Formulation

The experiments conducted in Chapter 3 were originally 3-phase experiments, but it was immediately evident that gas, water and oil flowing in a porous media were extremely complicated to understand let alone predict. In order to properly understand the system, 2-phase gas and water experiments were conducted. From previous research, it is known that a mobile gas phase in the presence of a mobile aqueous phase can induce mobility in an oil phase beyond its water-flood residual [35]. It is hypothesized that the gas phase in some way carries or displaces oil during this process. With knowledge of gas phase mobility in porous media it is possible to determine the oil phase mobility. An objective of this chapter is to modify Stone's Method applicable to oil phase mobility in 3-phase systems so that it is predictive for 3-phase systems under the influence of SWI.

The approach is based on the following premises: (1) Using the simulation of 2-phase systems an understanding was developed of gas and aqueous phase interactions in unconsolidated porous media. It is hypothesized that a third phase will not considerably affect the interaction and mobility of the aqueous and gas phases. If this hypothesis holds, it will be possible to characterize the mobility and flow of oil in a 3-phase system. (2) An adjustable function will be used instead of Stone's method due to its inadequacy in the experimental range. The function which determines oil phase mobility is dependent on the 3-phase saturation distribution. Consequently, it depends on adjustable parameters such as oil phase water flood residual S_{nqr}, critical oil phase residual S_{nrc}, and residual gas phase saturation S_{gr}. Experimental data will be used to calibrate each simulation to develop a model capable of predicting future 3-phase systems.

4.1.1 Experimental Methods

Chapter 4 experiments were conducted with the same laboratory equipment as the Chapter 3 experiments. The column is prepared in a manner consistent with that of Chapter 3. When the column properties are known the system is flooded with oil by adding kerosene to the top of the column and allowing water to drain from the bottom. This creates a system with water at its irreducible level and the remaining pore space occupied by oil. The irreducible water saturation has been independently determined by Leverett for sand and Ioannidis for glass bead systems and refers to the minimum water saturation that can be achieved, via drainage in this case. The system was then flooded with water, first at 1 mL/min and then 3 mL/min both until a pore volume has been injected into the column, effectively displacing some oil from the system and entrapping oil in the form of ganglia throughout the porous media. The oil saturation at the completion of this process is known as the water flood residual oil saturation. Figure 12 depicts the experimental setup.

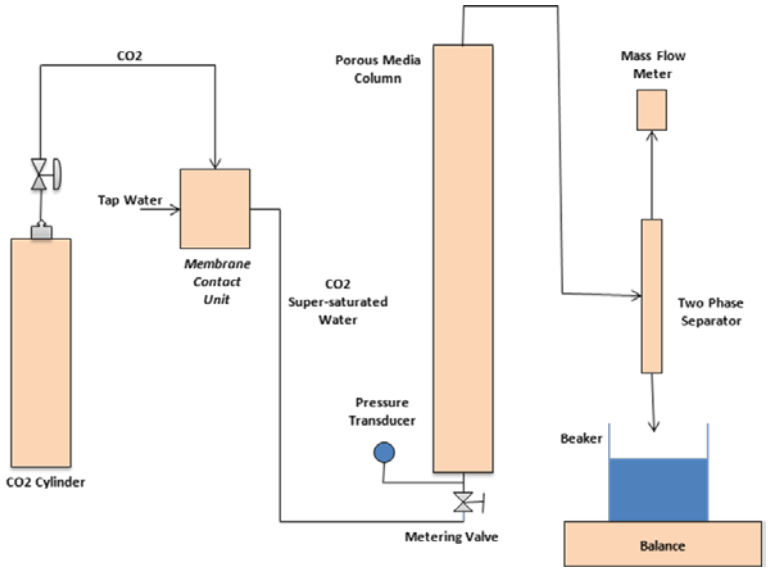

Figure 12: Experimental setup.

During SWI, aqueous, oil and gas phase effluents from the column were sent to a graduated pipette acting as a phase separator. The gas phase flows to the top of the separator through a mass flow meter and the liquid phases remain in the glass pipette. Due to buoyancy, the oil floated on top of the water where its volume was measured using a calibrated pipette. Water was collected from the base of the separator in a beaker and weighed continuously using a digital balance connected to a computer. A mass flow meter (Omega, model FMA3304), used to measure the effluent rate of the gas which

consisted of almost pure CO_2 and a pressure transducer (Validyne, model DP10-44) used to monitor the aqueous phase pressure at the base of the column were also interfaced with a computer.

At the start of each experiment, the column was maintained at zero gas saturation and at water flood residual oil saturation with the remaining pore space occupied by aqueous phase. Upon initiation of SWI, the supersaturated aqueous phase enters the column and carbon dioxide bubbles instantaneously form via nucleation; mass transfer to the gas phase continues until the gas phase pressure exceeds entrapping capillary pressures to allow for gas phase mobilization, fragmentation and coalescence as discussed in Chapter 3. The developing gas phase volumetrically displaces both trapped oil and free aqueous phase along its path causing flow throughout the column. Due to its connected nature, the aqueous phase is easily displaced and an increase in aqueous phase effluent is observed during the development of gas phase saturation. The disconnected oil phase does not immediately allow free-phase oil to flow out of the system; however, experimental results indicate that the oil phase is mobilized during the early stages of gas saturation development.

Experimental focus is divided into two areas of interest: short term gas saturation development and long term oil recovery. Short term experiments focus on a large number of measurements made over the time taken to produce gas saturation throughout the column, which is typically less than 1 pore volume injected. During this time, the average gas saturation of the column can be determined based on the aqueous phase effluent as detailed in Chapter 3. Long-term experiments focus on the ability of SWI to mobilize the oil phase contained in unconsolidated porous media. When the long-term experiments were conducted, the importance of data collection over the first pore volume injected was not known; subsequently gas phase saturation was not measured. Short-term experiments were used to calibrate gas phase relative permeability parameters to produce accurate long-term simulations. Long-term experiments are conducted until a large amount of oil phase is collected and the oil phase mobility is reduced near zero, typically over the injection of 100-200 pore volumes. Experimental data can be found in Tables 6 and 7.

4.1.2 Aqueous/Gas Phase Relative Permeability

Aqueous k_{rq} and gas k_{rg} phase relative permeability data for both the sand and glass bead packs were represented as follows [31]:

$$k_{rq} = \left(\frac{S_q - S_{qr}}{1 - S_{qr}}\right)^{n_q}$$

$$k_{rg} = \left(\frac{S_g - S_{gr}}{1 - S_{gr}}\right)^{n_g} \quad (18)$$

where S_{qr} and S_{gr} are the residual aqueous and gas phase saturations, respectively. Aqueous phase relative permeability parameters S_{qr} and n_q for packs of sand and glass beads were taken from the experimental works of Leverett [23] and Ioannidis et al. [12], respectively. Conversely, gas phase relative permeability parameters have been approximated for 2-phase systems in Chapter 3 and shown to be insensitive to unconsolidated porous media material; however, this study will show that gas phase mobility is sensitive to the presence of oil in a 3-phase system. The gas phase relative permeability parameters S_{gr} and n_g were estimated in this study and can be found in Table 2. Aqueous and gas phase relative permeability functions are shown in Figure 13.

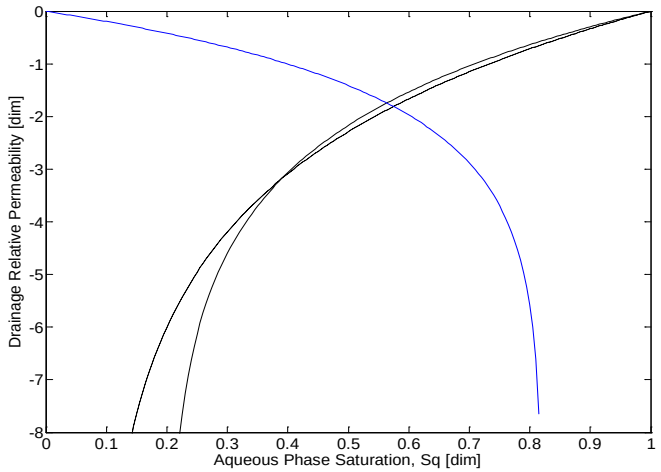

Figure 13: Aqueous and gas phase relative permeability curves.

Aqueous phase relative permeability is shown in black lines for sand (solid) and glass beads (dashed), whereas gas phase relative permeability is illustrated with a blue solid line. From the simulations, it is apparent that 3-phase gas mobility can be accurately modeled by slightly altering the 2-phase gas phase relative permeability function proposed in Chapter 3. By changing the residual gas saturation, S_{gr}, the simulation is able to achieve accurate gas saturation, mobility and effluent rates throughout the entirety of experiment. As shown in Table 3, the value of S_{gr} obtained for both sand and glass bead is 0.18, which is higher than the value obtained for the 2-phase case. It is not precisely known why the residual gas saturation increases when 3-phases are present; however, it is likely that the presence of the oil

phase in unconsolidated porous media disrupts gas phase flow. Due to their disconnected nature, oil ganglia are difficult to displace in the subsurface and may increase the overall resistance to gas flow.

4.1.3 Oil Phase Relative Permeability Function

Oil phase relative permeability in 2-phase systems has been studied considerably; however, it has not been sufficiently studied for 3-phase (oil, gas and water) systems. One study of particular importance to the petroleum industry led to Stone's development of a 3-phase oil relative permeability function [17].

$$k_{rn} = k_{rncq}\left\{\left(\frac{k_{rnq}}{k_{rncq}} + k_{rq}\right)\left(\frac{k_{rng}}{k_{rncq}} + k_{rg}\right) - \left(k_{rq} + k_{rg}\right)\right\} \tag{19}$$

where k_{rncq} is the constant oil relative permeability at connate water conditions, k_{rnq} is the oil relative permeability on the oil-water Corey curve, k_{rq} is the aforementioned aqueous phase relative permeability, k_{rng} is the oil relative permeability on the oil-gas Corey curve, and k_{rg} is the aforementioned gas phase relative permeability [17].

To accurately predict oil mobility in three phases, Stone proposed that events at both oil-water and oil-gas interfaces play roles which in turn implies that oil mobility is dependent on oil, gas, and aqueous phase saturations at any given time and position. Stone proposed a method for determining oil relative permeability that has been the cornerstone of 3-dimensional 3-phase modeling since its development and has been validated in a comprehensive literature review by Fayers and Matthews [35]. Unfortunately, the method has only been verified in high oil saturation and high gas saturation systems. During SWI, the system will typically achieve gas saturation no higher than 30% and oil saturation near water flood residual values less than 20%. Unfortunately, literature data associated with Fayers' and Matthews' review dealt with oil mobility in regions of high gas saturation and/or high oil saturation, regions which are not applicable to SWI in this study. The simulation was unable to reproduce experimental SWI results when using Stone's method to determine oil phase mobility. Numerically, Stone's method is not stable in the saturation range achieved by SWI in 3-phase systems because it does not smoothly approach a value of zero at low oil saturations; instead, the method produces negative values that have no physical representation.

To remedy the inadequacies of Stone's method, this paper will introduce a new relative permeability function that allows for accurate simulation of long-term SWI experiments and also approximates Stone's method at the conditions for which it has been shown to be valid. A function was developed on

the basis of two main contributions to oil mobility: 1) the 2-phase oil-water relative permeability table contributes to the mobility of the oil phase when saturations are above water flood residual levels and 2) a mobile gas phase in the presence of a mobile aqueous phase increases the oil phase mobility in unconsolidated porous media. This function is introduced in equations 20-21.

$$k_{rn} = k_{rnq} + \Omega_{Snrc} \cdot k_{rg} \cdot k_{rnc} \tag{20}$$

where,

$$k_{rnq} = \left(\frac{S_n - S_{nqr}}{1 - S_{nqr}}\right)^{n_n} \tag{20a}$$

$$\Omega_{Snrc} = (1 - k_{rnc}) \cdot \left(1 - k_{rg}\right) \cdot \Lambda \tag{20b}$$

$$k_{rnc} = \left(\frac{S_n - S_{nrc}}{1 - S_{nrc}}\right)^{n_n} \tag{20c}$$

Equation 20 (with equations a, b and c) determines the oil phase mobility based on a 2-phase system, k_{rnq}, with the added effects of gas phase mobility for a 3-phase system, Ω_{Snrc}-k_{rg}-k_{rnc}. The value k_{rnc} is the critical oil relative permeability developed for this study, and Ω_{Snrc} is a multiplier to determine the effect of gas phase mobility on oil phase mobility and was also developed for this study. The value S_{nqr} is the water flood residual saturation of oil and S_{nrc} is the critical residual saturation of oil, which is less than S_{nqr} during SWI. S_{nrc} is a parameter introduced in this study and was experimentally inferred; experiments appear to produce significantly less oil effluent when residual oil content is close to 6% for all experiments, which may indicate a lower boundary to the success of this technology. The value Λ is an adjustable parameter introduced to control the effect of gas phase mobility on oil phase mobility in the model. Oil phase mobility as predicted by the oil-water Corey curve, k_{rnq} , will not be affected unless the gas phase present in the system is mobile, which is consistent with previous research [36]. Due to the complexity of the system, a modifiable multiplier such as Ω_{Snrc} was required because a single set of parameters was not able to simulate all long-term oil experiments. It was necessary to control gas phase mobility effects on oil phase mobility for each experiment in order to accurately fit experimental data.

4.2 Results and Discussion

In the simulations reported here, only the gas relative permeability parameter S_{gr} and the oil relative permeability parameters S_{nrc} and Λ were considered adjustable. Every other parameter was independently measured or estimated, similar with the previous chapter except the value n_g was assumed from Chapter 3. In what follows, the observations and numerical results which pertain to the short-term and long-term experiments are discussed. Short-term experimental results include the first 2 pore volumes injected during the long-term experiments; therefore, it is hoped that the short-term experimental results can be used to better understand the long-term experiments. Subsequently, continuum model predictions for both short and long term experiments are delineated.

4.2.1 Short-term Experiments and Simulations

Short term experiments were designed to collect large amounts of data during the development of gas saturation throughout the column. Study of this timeframe is necessary to properly understand how the presence of an oil phase changes the gas phase characteristics from a 2-phase system to a 3-phase system. The history of one short term experiment can be observed in Figure 14.

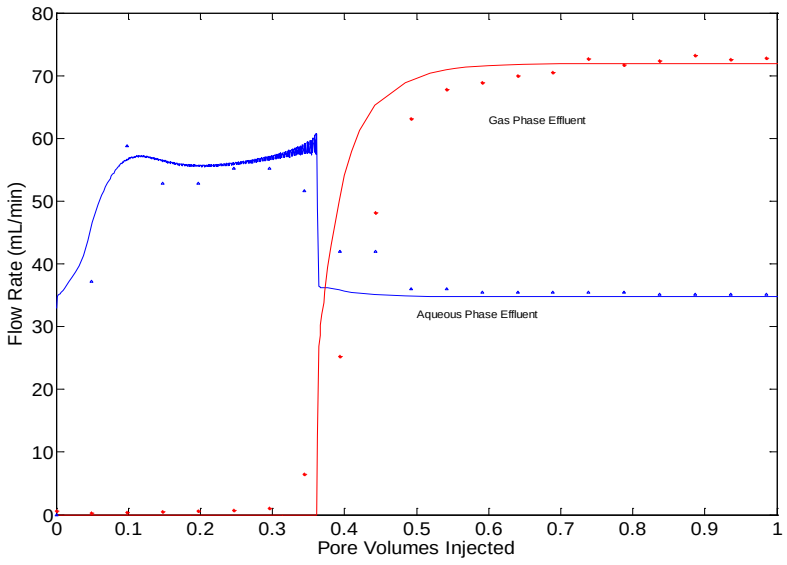

Figure 14: Experiment 15 short-term gas and aqueous phase effluent curves.

It is apparent that the fitted model is capable of reproducing the aqueous and gas phase effluents in a 3-phase system. However, short-term calculations have indicated that the gas phase mobility in a 3-phase

system differs from that in the 2-phase experiments. To properly fit both short and long term experiments, the gas phase relative permeability curve had to be slightly adjusted using experimental calibration. Although this may seem a small detail of the experiment, it may in fact provide a clue as to how the oil phase is mobilized by the presence of a mobile gas phase. The 3-phase experiments show a significant increase in gas phase saturation, which indicates that the presence of the oil phase is restricting gas phase flow. In Experiment 8 (2-phase) the gas phase effluent is around 58 mL/min producing an average gas phase saturation of 14-15%, whereas Experiment 15 (3-phase) has a gas phase effluent of only 50 mL/min producing an average gas saturation of 21-22%. Explanations for this observation include reduced hydraulic conductivity during volumetric displacement of aqueous phase by gas phase, oil phase ganglia disrupting gas flow channel creation and difficulties displacing ganglia due to their disconnected nature. Each aforementioned explanation would result in an increase in entrapping pressure of a gas bubble inside a pore, which could cause an increase in capillary pressure and result in higher gas phase saturation.

During short-term experiments, the oil phase was mobilized as shown in figure 15.

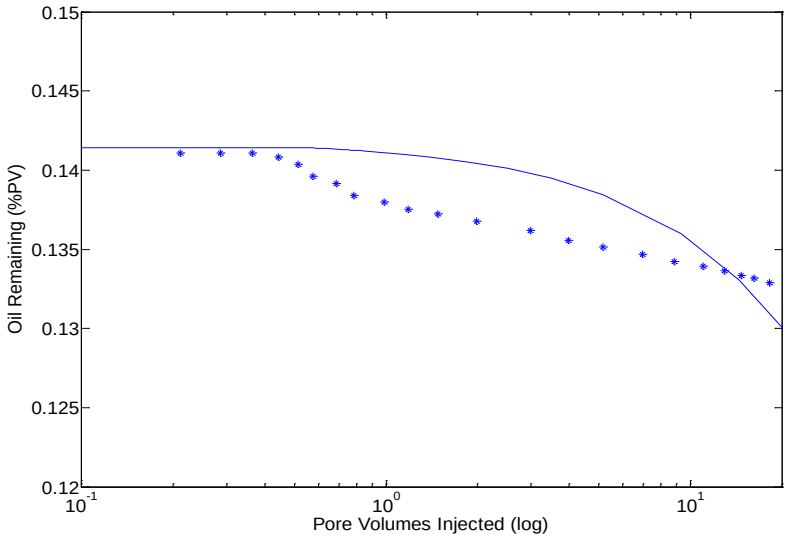

Figure 15: Experiment 15 short-term oil recovery experiment and simulation.

During the first pore volume injected there is a measureable and relatively large volume of oil phase effluent. The oil effluent is likely caused by oil bank formation along the developing gas saturation front that is described in Chapter 2. As the gas phase first moves through the column it volumetrically displaces and redistributes both oil and aqueous phases. By redistributing disconnected ganglia, it is possible that buoyant clusters can form and be propelled out of the system buoyantly, by the gas

saturation front. The oil phase effluent is produced at the same time as the first gas phase effluent, which is sufficient evidence to support this theory.

Figure 15 shows that oil phase recovery during this time is not accurately computed by the model. The relative permeability function as described in Section 4.1.2 was designed to incorporate oil mobility for 2-phase oil-water systems and include the effects of gas phase mobility on the oil phase mobility in 3-phase systems. Unfortunately, the factors affecting oil phase mobility are likely dynamic and so can change throughout long-term experiments. It is possible to accurately model both short-term and long-term oil production; however, this would require the use of a step function and further complicate the simulation. Concessions were made to focus on long-term oil recovery instead because field-scale applications typically last much longer than 10 pore volumes.

4.2.2 Long-term Experiments and Simulations

Long-term experiments were designed to collect large amounts of data throughout an experiment consisting of more than 200 pore volumes injected. Study of this timeframe is necessary to properly understand how the introduction of mobile gas and aqueous phases via SWI can produce mobility in an otherwise immobile disconnected oil phase. The results contained in the long-term experiments can be found in Table 7. The variations of oil-phase saturations obtained during these experiments are shown in Figure 16.

The aqueous and gas phase effluents are not displayed because they are not the focus of this time period, but they were accurately by the model. Relative permeability and continuum-scale concepts are not capable of exactly modeling the dynamics observed during experiment; however, concessions must be made in order to scale a pore-scale process up to the continuum-scale. Each long-term experiment has been accurately predicted by simulation; however, all of the experiments could not be predicted by a single relative permeability function. Table 8 shows simulation characteristics and model parameters obtained for each experiment. Model parameters such as Λ are able to control the effect that gas phase mobility has on the oil phase.

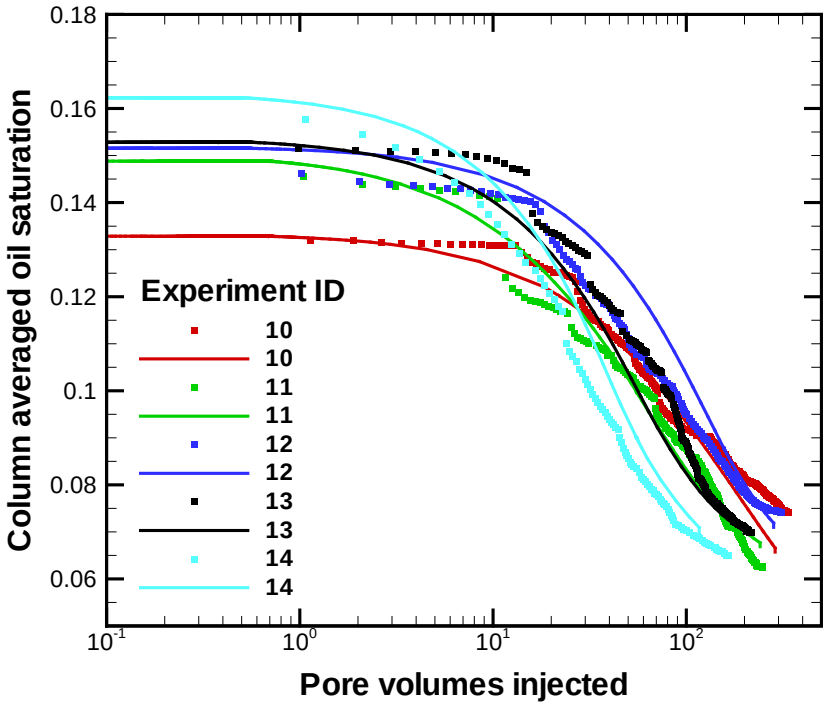

Figure 16: Experiments 10-14 long-term oil recovery experiments (solid lines) and simulations (symbols).

Figure 16 show that consistent oil effluent curves are obtained for the various experiments, which allow continuum-scale relative permeability concepts to be used. It is apparent that gas phase mobility and oil phase mobility are highly correlated, but the physical mechanism at work is not completely understood. A high density band of results and simulations, which is indicative of the high correlation between gas phase and oil phase mobility. The figure is a normalized representation of experimental and simulation results; it also indicates a very strong relationship between percent of oil phase remaining and pore volumes of aqueous phase injected.

Although the end-point average oil phase saturation is accurately simulated for each experiment, effluent observations are unable to show the remaining oil distribution in the column at the end of an experiment. To truly determine if the simulation is capable of predicting oil phase flow, the residual saturations throughout the column must be matched. To determine the end of experiment saturation gradient, porous media were carefully removed from the column and analyzed with gas chromatograph technology, as detailed in Li [36]. The columns were later reconstructed virtually with average oil saturation data at the various locations. One such reproduction can be found in Figure 17.

The nearly homogeneous distribution of oil phase at the end of SWI experiments matches simulation results very well. Experimental results are consistent with simulation techniques; however, the simulation is forced to produce a nearly homogeneous end-point by boundary conditions and assumptions such as a critical saturation for oil mobility, S_{nrc}.

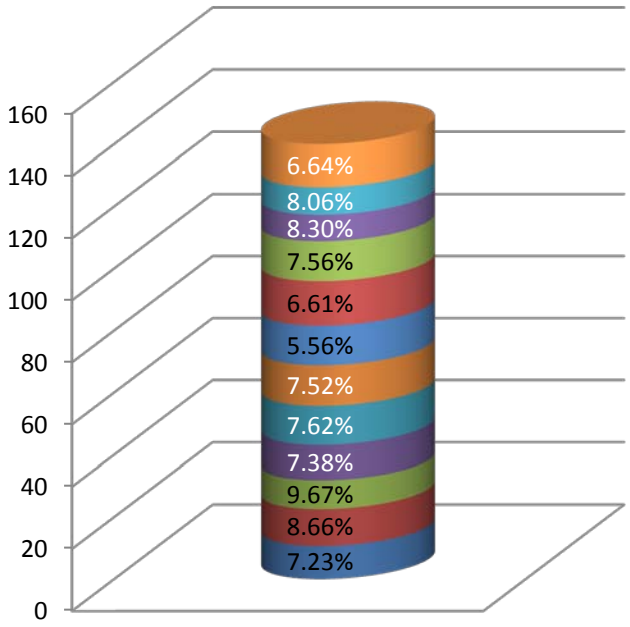

Figure 17: Example of saturation distribution produced at end of SWI oil recovery [36].

4.2.3 Enouy Approximation of Stone's Method

The main goal of this paper is to produce a function capable of predicting oil mobility at low oil saturations during SWI; however, a function capable of predicting oil mobility for all saturations of gas, oil and water phases would be more useful. Isoperm Contour plots of Stone's Method and the Enouy approximation of Stone's Method were created to show their similarities. Figure 18 shows the dependence of k_{rn} on oil and gas-phase saturations based on Stone's Method, while Figure 19 presents the results obtained using the Enouy Approximation.

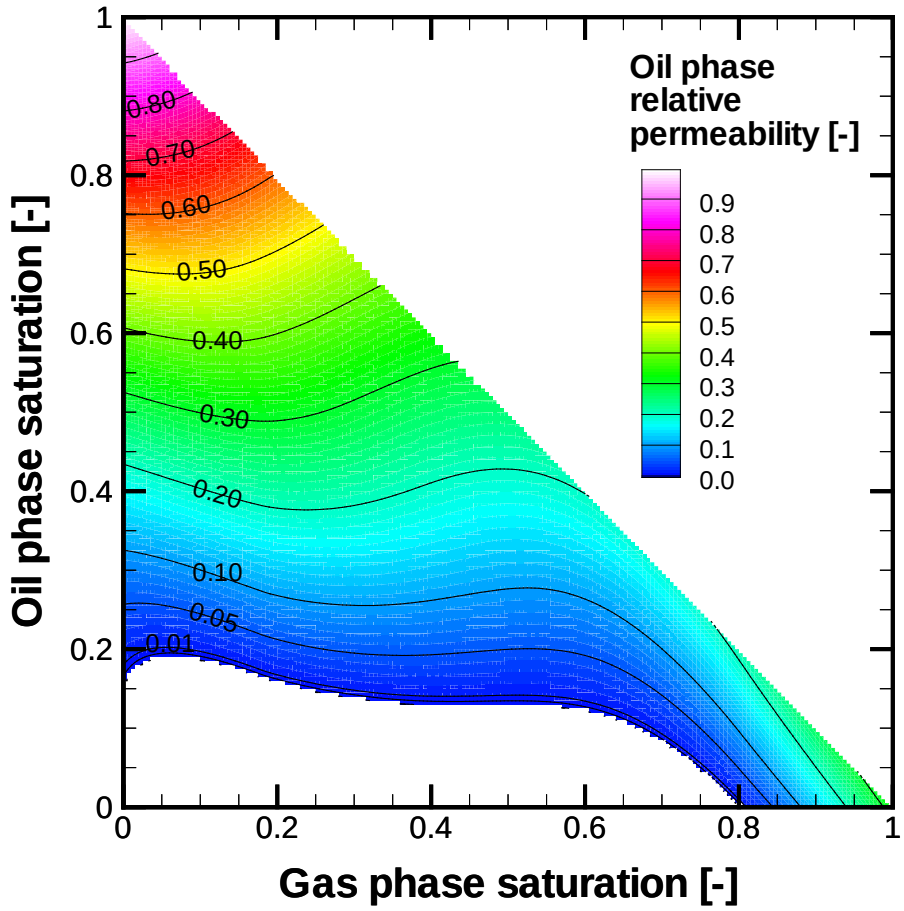

Figure 18: Stone's Method for producing oil phase relative permeability in 3-phase systems.

$$S_{rn} = 0.14, S_{rq} = 0.20, S_{rg} = 0.18, k_{rncq} = 0.6723, k_{rng} = \left(\frac{S_n - 0.20}{1 - 0.20}\right)^{1.8}$$

Simulations were conducted with Stone's Method approach for determining relative permeability of oil phase in 3-phase systems; however, any oil mobility that was created was large enough to predict all oil effluent within the first 10 pore volumes. Stone's Method cannot predict SWI experiments for flow in 1D columns.

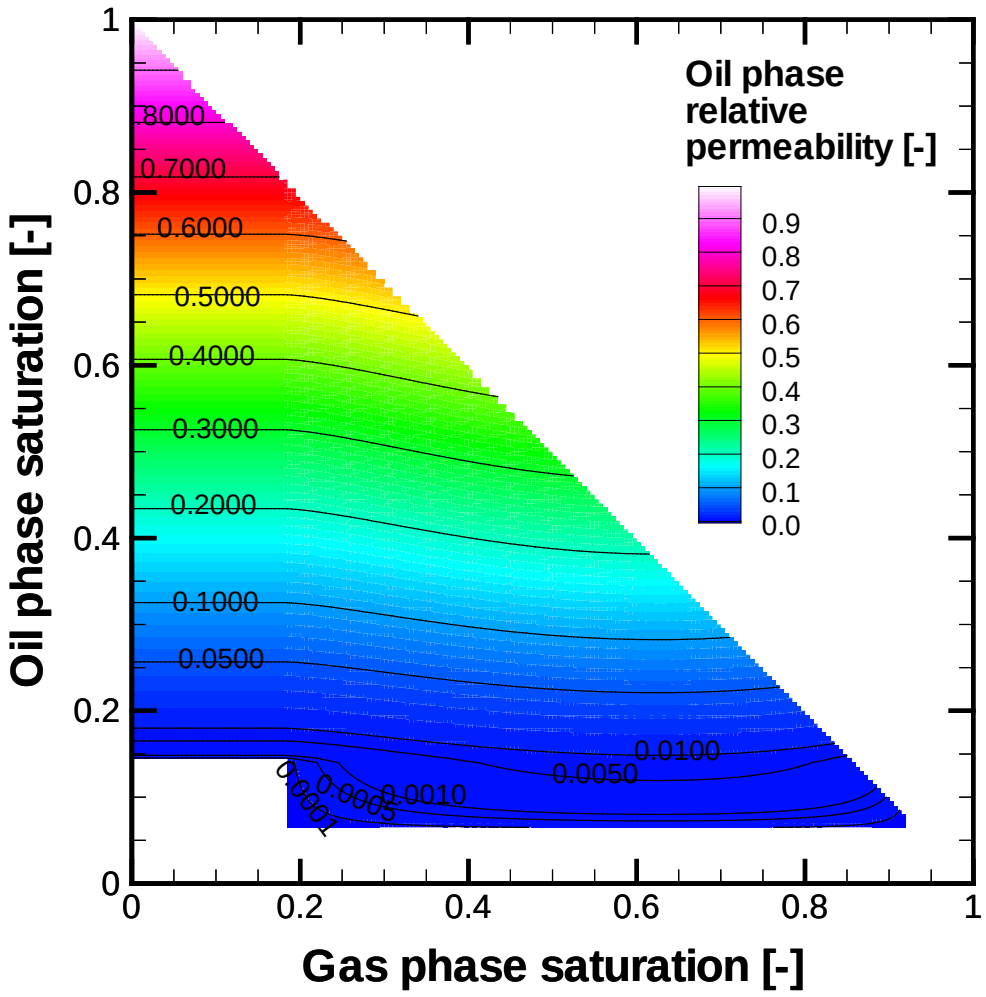

Figure 19: Enouy approximation of Stone's Method for oil phase relative permeability in 3-phase systems.

$\boldsymbol{S_{nqr} = 0.14, \Lambda = 2.0, S_{nrc} = 0.06}$.

By comparing the figures side-by-side it is difficult to tell how similar the two methods are; however, a third contour plotting the absolute difference of Enouy and Stone can be found in Figure 20.

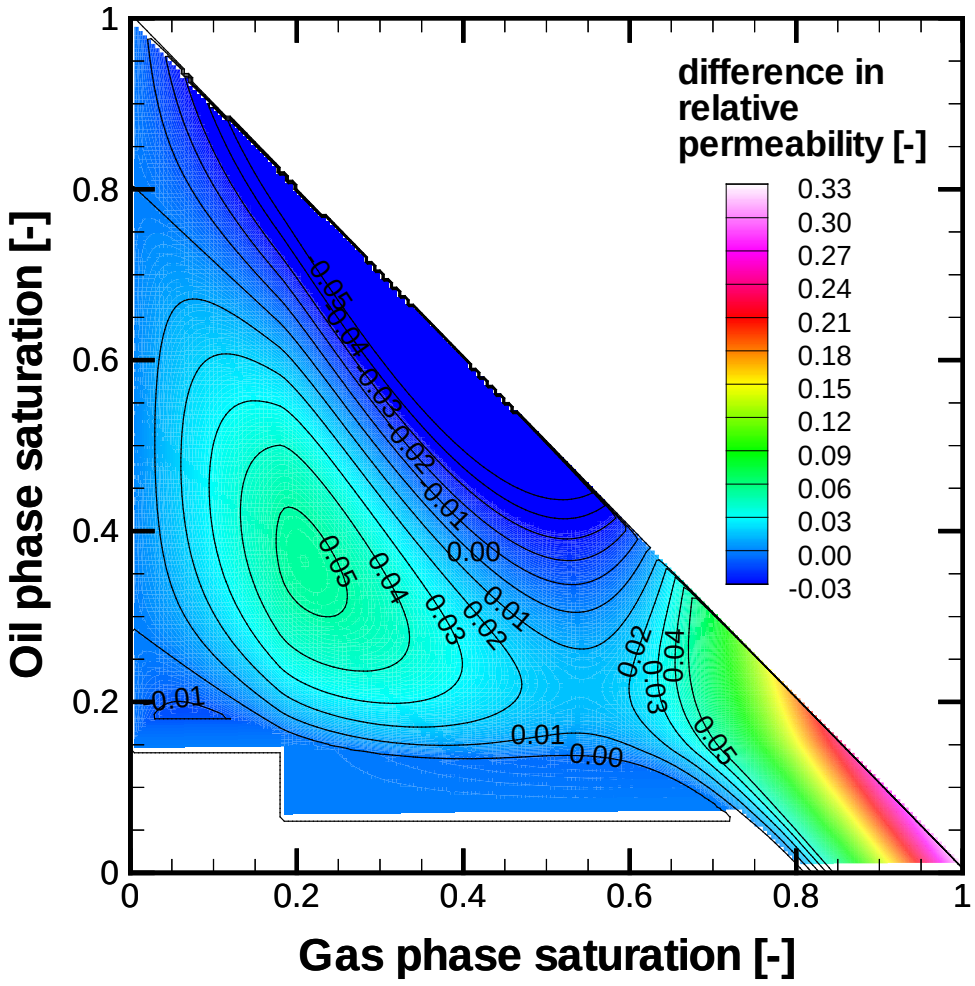

Figure 20: Difference between Enouy approximation and Stone's Method for oil phase relative permeability in 3-phase systems.

The majority of contour lines, and therefore difference between the methods are smaller than 0.06, a reasonable difference, which is a testament to the similarity between the two methods. Obviously, the difference between the methods is large at low oil and high gas saturations – the region in which Stone's Method performs poorly.

$$\boldsymbol{Difference} = \boldsymbol{k_{nr,Stone}} - \boldsymbol{k_{nr,Enouy}} \quad (21)$$

Table 6: Properties of packed columns SWI experiments.

Experiment ID	Packing	Permeability K [darcy]	Porosity ϕ [−]	Water Flood Residual Oil S_{nqr} [-]
10	Sand	11.4	0.387	0.133
11	Sand	09.1	0.369	0.149
12	Sand	31.2	0.380	0.152
13	Sand	29.4	0.350	0.153
14	Sand	41.9	0.358	0.162
15	Sand	44.8	0.365	0.141
16	Glass beads	64.4	0.395	0.134

Table 7: Experimental observations.

Experiment ID	Duration	Q_{q-avg}^{inj} [mL/min]	Q_{g-avg}^{eff} [mL/min]	$\overline{S}_g$[−]	Fraction Oil Recovery [%]
10	Long	35.2	67.6	-	0.442
11	Long	28.5	56.6	-	0.581
12	Long	25.6	53.2	-	0.511
13	Long	26.5	58.1	-	0.590
14	Long	26.3	56.6	-	0.599
15	Short	23.7	50.9	0.214	0.060
16	Short	24.3	50.6	0.198	0.047

Table 8: Simulation results and parameters.

Simulation ID	Duration	$\overline{S}_g[-]$	Fraction Oil Recovery [%]	Oil Mobility Multiplier $\Lambda[-]$
10	Long	0.197	0.453	2.5
11	Long	0.199	0.551	6
12	Long	0.203	0.532	2
13	Long	0.205	0.626	4.5
14	Long	0.203	0.574	5
15	Short	0.201	0.075	2
16	Short	0.198	0.055	2

Chapter 5

5. Conclusions

5.1 Gas Exsolution and Flow during Supersaturated Water Injection in Porous Media

A first investigation of the process is conducted of CO_2-supersaturated water injection (SWI) in water-saturated porous media by means of experiments in homogeneous columns packed with glass beads or silica sand and continuum-scale simulation. This study addressed aspects of two-phase flow and mass transfer at the macroscopic scale, strengthening and extending a number of conclusions reached in the first part of this work [1], where CO_2-supersaturated water injection was studied by pore network simulation. A multiphase compositional model (CompFlow-SWI) was employed to interpret the experimental observations, leading to the following conclusions:

- Initial formation (nucleation) and growth of the CO_2 gas phase during SWI is associated with the development of an exsolution zone of finite extent near the point of injection. Rate-limited transfer of CO_2 from the aqueous to the gas phase is adequately described at the macroscopic scale by a published correlation due to Nambi and Powers [19].
- Gas phase accumulating within the exsolution zone becomes mobile at a critical value of gas saturation which, for the media studied in this work, is close to the breakthrough gas saturation for drainage of the aqueous phase (*ca.* 0.14). Advection of the gas phase is consistent with the advancement of a sharp front and can be predicted by the classical extension of Darcy's law to two-phase flow. The associated gas phase relative permeability is determined and found to be insensitive to changes in particle size and injection flow rate.

The finding that displacement of the aqueous phase by gas is compact at the macroscopic scale is consistent with a pore-level description of the SWI process, according to which gas phase propagation under conditions of small Bond number results from repeated mobilization, fragmentation and coalescence of large gas clusters (i.e., large ganglion dynamics) driven entirely by mass transfer. The apparent success of a Darcy-based model of gas phase mobility hinges on the existence of a representative elementary volume (REV) for gas saturation, which is assured by the uniform nature of

nucleation and mass transfer-driven growth of a gas phase in porous media. This is likely a significant advantage of SWI over gas sparging, which generally results in channelized gas flow.

5.2 Oil Recovery and Flow during Supersaturated Water Injection in Porous Media

An investigation was conducted to determine how the process of CO_2-supersaturated water injection (SWI) can produce mobility in a disconnected oil phase that was previously immobile. Experiments were carried out in homogeneous columns packed with both silica sand and glass beads with a water flood residual oil phase; SWI was initiated to produce oil, gas and aqueous phase effluents and was used to calibrate a continuum-scale simulation. This study addressed aspects of 3-phase flow during SWI that has not been previously investigated. A new relative permeability relationship for gas phase in the presence of oil and water was developed, which is slightly different from the relationship developed for 2-phase flow. Stone's method for 3-phase oil relative permeability was shown to be inadequate for simulating SWI systems and a new function was developed. The function accurately predicts relative permeability in areas where Stone is valid as well as the low oil saturations applicable to SWI. A multiphase compositional model (CompFlow-SWI) was employed to interpret the experimental observations, leading to the following conclusions:

- Gas phase flow in porous media was shown to be sensitive to the presence of an oil phase for both sand and glass bead packed columns. The average gas phase saturation was much higher for 3-phase systems than 2-phase systems. The relative permeability curve for gas phase flow had to be altered in order to match experimental results, but the new relationship was able to accurately predict each 3-phase experiment. It is concluded that a residual disconnected oil phase increases resistance to gas phase flow, although the exact mechanism is yet unknown.
- Oil phase flow cannot be adequately described by Stone's Method during SWI. To allow for accurate reproduction of experimental results a new relative permeability function was developed. The new function is able to accurately predict oil relative permeability as the oil phase approached immobile saturations. The function is also able to accurately reproduce Stone's Method predictions for high oil saturations and high gas saturations.

A disconnected oil phase can be mobilized with supersaturated water injection and accurately predicted with a continuum-scale modeling approach.

References

1. Zhao W, Ioannidis MA. Gas exsolution and flow during supersaturated water injection in porous media: I. Pore network modeling, submitted for publication.
2. Avraam DG, Payatakes AC. Flow regimes and relative permeabilities during steady-state 2-phase flow in porous media. J Fluid Mech 1995; 293:207-236.
3. Avraam DG, Payatakes AC. Generalized relative permeability coefficients during steady-state 2-phase flow in porous media and correlation with the flow mechanisms. Transp Porous Media 1995; 20:135-168.
4. Fry VA, Selker JS, Gorelick SM. Experimental investigations for trapping oxygen gas in saturated porous media for in situ bioremediation. Water Resour Res 1997; 33(12):2687-2696.
5. Li TMW, Ioannidis MA, Chatzis I. Recovery of non-aqueous phase liquids from ground sources. United States patent #7300227, 2007.
6. Bass DH, Hastings NA, Brown RA. Performance of air sparging systems: a review of case studies. J Hazard Mater 2000; 72:101-119.
7. Nelson LC, Barker J, Li T, Thomson N, Ioannidis M, Chatzis I. A field trial to assess the performance of CO_2-supersaturated water injection for residual volatile LNAPL recovery. J Contam Hydrol. 2009; 109:82-90.
8. Brooks MC, Wise WR, Annable MD. Fundamental changes in in-situ air sparging flow patterns. Ground Water Monit Rem 1999; 19(2):105-113.
9. Chen M-R, Hinkley RE, Killough JE. Computed tomography imaging of air sparging in porous media. Water Resour Res 1996; 32(10):3013-3024.
10. Elder CR, Benson CH. Air channel formation, size, spacing and tortuosity during air sparging. Ground Water Monit Rem 1999; 19(3):171-181.
11. Geistlinger H, Lazik D, Krauss G, Vogel H-J. Pore-scale and continuum modeling of gas flow pattern obtained by high-resolution optical bench-scale experiments. Water Resour Res 2009; 45. doi:10.1029/2007WR006548.
12. Ioannidis MA, Chatzis I, Lemaire C, Perunarkilli R. Unsaturated hydraulic conductivity from nuclear magnetic resonance measurements. Water Resources Research 2006; 42: W07201, doi:10.1029/2006WR004955.
13. Johnson RL, Johnson PC, McWhorter DB, Hinchee RE, Goodman I. An overview of in situ air sparging, Ground Water Monit Rem 1993; 13(4):127-135.

14. Selker JS, Niemet M, McDuffie NG, Gorelick SM, Parlange JY. The local geometry of gas injection into saturated homogeneous porous media. Transp Porous Media 2007; 68(1):107-127.
15. Stauffer F, Kong XZ, Kinzelbach W. A stochastic model for air injection in porous media. Adv Water Resour 2009; 32(8):1180-1186.
16. Stohr M, Khalili A. Dynamic regimes of buoyancy-affected two-phase flow in unconsolidated porous media. Phys Rev E 2006; 73:art. No. 036301.
17. Stone HL. Estimation of three-phase relative permeability and residual oil data. Journal of Canadian Petroleum Technology, Oct-Dec 1973; 53-60.
18. Forsyth PA, Unger AJA, Sudicky EA. Nonlinear iteration methods for nonequilibrium multiphase subsurface flow. Adv Water Resour 1998; 21:433-449.
19. Nambi IM, Powers SE. Mass transfer correlations for nonaqueous phase liquid dissolution from regions with high initial saturations. Water Resour Res 2003; 39(2):1030, doi:10.1029/2001WR000667.
20. Kashchiev D, Firoozabadi A. Kinetics of the initial stage of isothermal gas phase formation. J Chem Phys 1993; 98(6):4690–4699.
21. Forsyth PA. A positivity-preserving method for simulation of steam injection for NAPL site remediation. Adv Water Resour 1993; 16:351-370.
22. Unger AJA, Forsyth PA, Sudicky EA. Influence of alternative dissolution models and subsurface heterogeneity on DNAPL disappearance times. J Contam Hydrol 1998; 30:217-242.
23. Leverett MC. Capillary behaviour in porous solids. Trans AIME 1941; 142:159–172.
24. D'Azvedo EF, Forsyth PA, Tang W-P. Towards a cost-effective high order ILU preconditioner. BIT 1992; 32:442-463.
25. Saad Y, Schultz M. GMRES: a generalized minimum residual algorithm for solving nonsymmetric linear systems. SIAM J Sci Statist Comp 1986; 7:856-869.
26. Van der Vorst HA. Bi-CGSTAB: a fast a smoothly converging variant of BiCG for the solution of nonsymmetric linear systems. SIAM J Sci Statist Comp 1992; 13:631-645.
27. Smith, Van Ness and Abbott. Introduction to Chemical Engineering Thermodynamics. New York, NY: McGraw-Hill, 2005. Print.
28. Felder, Richard M., and Ronald W. Rousseau. Elementary Principles of Chemical Processes. New York: John Wiley, 2000. Print.
29. Hines, Anthony L., and Robert N. Maddox. Mass Transfer: Fundamentals and Applications. Englewood Cliffs, NJ: Prentice-Hall, 1985. Print.

30. Oxtoby, Gillis and Nachtrieb. Principles of Modern Chemistry. Toronto, CA: Thompson Learning, 2002. Print.
31. Corey AT. The interrelation between gas and oil relative permeabilities. *Prod. Mon*. 1954; 19(1):38-41.
32. Li X, Yortsos YC. Visualization and simulation of bubble growth in pore networks. AIChE J 1995; 41(2):214-222.
33. Thomson NR, Johnson RL. Air distribution during in situ air sparging: an overview of mathematical modeling. J Hazard Mater 2000; 72:265-282.
34. Tsimpanogiannis IN, Yortsos YC. The critical gas saturation in a porous medium in the presence of gravity. J Colloid Interface Sci 2004; 270 (2):388-395.
35. Fayers and Matthews. Evaluation of Normalized Stone's Methods for Estimating Three-Phase Relative Permeabilities. Soc of Petro Eng Journal, April 1984; 224-231.
36. Li M. Recovery of Non-aqueous phase liquids from contaminated soil by CO_2 supersaturated water injection. University of Waterloo, Master of Applied Science thesis, 2009.
37. Ji W, Dahmani A, Ahfeld DP, Lin JD, Hill E. Laboratory study of air sparging: Air flow visualization. Ground Water Monit Rem 1993; 13(4):115-126.
38. Klotz D, Seiler K-P, Moser H, Neumaier F. Dispersivity and velocity relationship from laboratory and field experiments. J Hydrol 1980; 45:169-184.
39. Buckley SE, Leverett MC. Mechanism of fluid displacements in sands. Trans AIME 1942; 146:107–116.